PROCEEDINGS, Forty-First Workshop on Geothermal Reservoir Engineering
Stanford University, Stanford, California, February 22-24, 2016
SGP-TR-209

An Assessment of Some Design Constraints on Heat Production of a 3D Conceptual EGS Model Using an Open-Source Geothermal Reservoir Simulation Code

Yidong Xia[a], Mitchell Plummer[a], Robert Podgorney[a], and Ahmad Ghassemi[b]

Idaho National Laboratory, 1955 N. Fremont Ave, P.O. Box 1625, Idaho Falls, ID 83415-2025

University of Oklahoma, 660 Parrington Oval, Norman, OK 73019

Corresponding E-mail address: yidong.xia@inl.gov

Keywords: EGS, heat production, fracture spacing, flow rate, finite element method

ABSTRACT

Performance of heat production process over a 30-year period is assessed in a conceptual EGS model with a geothermal gradient of 65K per km depth in the reservoir. Water is circulated through a pair of parallel wells connected by a set of single large wing fractures. The results indicate that the desirable output electric power rate and lifespan could be obtained under suitable material properties and system parameters. A sensitivity analysis on some design constraints and operation parameters indicates that 1) the fracture horizontal spacing has profound effect on the long-term performance of heat production, 2) the downward deviation angle for the parallel doublet wells may help overcome the difficulty of vertical drilling to reach a favorable production temperature, and 3) the thermal energy production rate and lifespan has close dependence on water mass flow rate. The results also indicate that the heat production can be improved when the horizontal fracture spacing, well deviation angle, and production flow rate are under reasonable conditions. To conduct the reservoir modeling and simulations, an open-source, finite element based, fully implicit, fully coupled hydrothermal code, namely FALCON, has been developed and used in this work. Compared with most other existing codes that are either closed-source or commercially available in this area, this new open-source code has demonstrated a code development strategy that aims to provide an unparalleled easiness for user-customization and multi-physics coupling. Test results have shown that the FALCON code is able to complete the long-term tests efficiently and accurately, thanks to the state-of-the-art nonlinear and linear solver algorithms implemented in the code.

1. INTRODUCTION

1.1 Background

The concept of Enhanced Geothermal Systems (EGS) (see Batchelor 1982, Cornet 1989), which includes the earlier concept of Hot Dry Rock (HDR) (see Smith et al. 1975, Tester et al. 1989, Duchane 1990, and Duchane et al. 2002), originated at the Los Alamos National Laboratory (LANL) in the 1970s, and has been widely studied and experimented in many countries over the last three decades. Since an abundance of literature that describes the basics of EGS can be found (for example, a comprehensive review on the EGS concept, recent development and future challenge is reported in Olasolo et al. 2016), it is not within the scope of this work to reiterate those contents. Research and development of the EGS has been increasingly popular recently, largely due to the U.S. Department of Energy's FORGE (Frontier Observatory for Research in Geothermal Energy) program. As pointed out in Olasolo et al. 2016, the key to the EGS financial viability is the ability to produce energy over long periods without the need to carry out expensive repairs such as the unplanned drilling of additional wells. Therefore an optimal technical design plan must be determined for an EGS plant at all stages of development and operation. For example, the correct placement of injection and production wells for the stage of heat extraction process is critical to the heat production performance of an EGS plant. However, a number of uncertain factors are still at large regarding the specific technical requirement for this stage of the EGS reservoir development, due to the lack of operational experience to date. As a matter of fact, most EGS plants are so new that their operations are measured in months rather than years in lots of cases. Owning to the many uncertainties associated to the EGS operation (U.S. Department of Energy 2008), the numerical simulation has been recognized and used as a relatively economical, robust, and reliable approach for the design of conceptual EGS models and validation of heat extraction performance.

1.2 Modeling of Heat Production in EGS

The interest of the present work is focused on the design of EGS well layout for long-term heat extraction performance. The EGS well layout schemes often modeled, simulated, and analyzed include these three types: 1) doublet (an injection and production well pair), 2) triplet (an injector flanked by a production well on each side), and 3) five-spot (an injector at the center and a production well at each corner of a square). Due to the huge volume of excellent works published on this topic, only some of the recent and related works are reviewed here. Sanyal et al. 2005 simulated the 30-year power generation period of a 3D hypothetical EGS model with a five-spot well layout, and analyzed its performance in terms of fracture spacing, reservoir permeability, and well geometry. Zeng et al. 2013(a) investigated the performance of a 2D conceptual EGS model with a horizontal doublet well layout, and affirmed that the energy efficiency mainly depends on the reservoir permeability and the water production rate. Later on, Jiang et al. 2014 designed and simulated the 40-year heat extraction period of a 3D conceptual EGS with a triplet well layout, and demonstrated that it is able to retain the preferential flow in the reservoir and significantly elongate the heat production performance by 10 years over its doublet counterpart. Chen et al. 2015 conducted a comparative study on long-term performance between the doublet well layout, two triplet well layouts, and a five-spot layout. Their numerical results showed that it does not necessarily improve the EGS performance by simply deploying more production wells, as an EGS with a triplet well layout can perform better than an EGS with a five-spot well layout or worse than an EGS with a doublet well layout. More recently, Chen at al. 2016 performed a detailed sensitivity study of the heat extraction process in a doublet well EGS in terms of a series of design parameters, and found that the EGS production temperature and lifetime are tightly related to the

flow pattern in the reservoir, while the thermal compensation from rocks surrounding the reservoir contributes little heat to the heat transmission fluid if the operation period is shorter than 15 years. Though most of these works were based on a hypothetical or conceptual EGS model, the rich experience gained through these studies has substantially advanced our understanding of optimization for EGS heat production performance, and paved our way for future research endeavors.

1.3 Numerical Methods and Simulation Codes

Numerical design of EGS models requires reliable numerical methods to simulate the coupled thermal-hydraulic-mechanical-chemical (THMC), or thermal-hydraulic-mechanical (THM), or thermal-hydraulic (TH) processes, depending on the multiphysics to be resolved in specific problems. A review on the recent progress of simulation technologies for coupled THMC and THM processes in EGS can be found in Xing et al. 2015. In this section, our focus is limited to some codes and their recent applications for modeling EGS long-term heat extraction dominated by the coupled TH processes, where the mechanical interaction between rock and fluid as well as the rock thermoelastic effect may be neglected. Zeng et al. 2013(a), Zeng et al. 2013(b), and Bujakowski et al. 2015 used the hydrothermal code, TOUGH2 (Pruess et al. 1999), for simulating the heat production from EGS models, respectively. However, the finite difference method (FDM) such as in TOUGH2 require high-quality structured meshes to obtain accurate solution, which largely limits the complexity of the fracture features to be modeled. Though the FDMs can handle irregular meshes, yet the use of irregular meshes could result in over-diffused solution with low accuracy ($\leq$ first order) for the convection-dominated heat transport in fractured reservoirs, which might lead to significant over-prediction of EGS production lifetime. Somehow, the inconvenience associated to the FDMs triggered people's desire to resort to unstructured mesh methods, such as the finite volume methods (FVMs) and finite element methods (FEMs). Based on the computational fluid dynamics (CFD) solver, Fluent®, Jiang et al. 2014 developed a 3D hydrothermal flow model that uses the cell-centered FVM for solving the transient incompressible flow and heat transfer with the Navier-Stokes (NS) equations in reservoirs and wells. It was then applied in an extensive study of EGS well layouts (Chen at al. 2015, and Chen et al. 2016). However, a caveat with this model is that Jiang et al. 2014 did not validate if their use of the first-order upwind differencing scheme for the discretization of spatial derivative terms was able to retain sufficient solution accuracy for simulating a long-term convective heat transport in fractured reservoir, though the first-order scheme essentially guarantees the total-diminishing variation (TVD) condition for the energy solution. Alternatively, the Galerkin FEMs and so-called "Control-Volume" FEM (CV-FEM, nothing but the node-centered FVM) may offer more flexibility for reservoir modeling, as they support the implementation of 1D, 2D, and 3D elements in the same model (e.g., in a 3D EGS model, the fractures can be represented with 2D planar surfaces embedded in 3D rock matrix, and the wells can be represented with 1D curves). Examples of the codes based on those methods include the FEHM code developed at LANL (Zyvoloski 2007), the FRACTure code by Kohl et al. 1995 and applied in Held et al. 2014, and the PANDAS code by Xing at al. 2015. Despite the advantages of treating complex geometric configurations, most Galerkin FEM and CV-FEM codes are so far not as powerful as the mature FDM code like TOUGH2 to model very complex THMC processes. Further numerical methods and code development for the Galerkin FEMs and CV-FEMs are in urgent demand to overcome their existing weaknesses, and improve our understanding, design, and operation of EGS.

1.4 Objectives

The main objectives to be discussed in the present work are two-fold. First, the performance of heat production process over a 30-year period from a conceptual EGS model is evaluated. In this model, the water is circulated through two horizontal wells connected by a set of single large wing fractures in a fully saturated geothermal reservoir field. The effects of some design constraint factors, such as the fracture horizontal spacing, flow rate, and well horizontal deviation angle on the EGS heat production performance are assessed. The production characteristics as well as the design and optimization of the doublet well layout are investigated in detail. Second, an open-source, space-time second-order Galerkin FEM based geothermal reservoir simulation code, namely FALCON (Fracturing And Liquid CONvection), is developed and employed for the simulation test cases in this work. Originally introduced in Podgorney et al. 2010, the closed-source FALCON code features a massively parallel, fully implicit, and fully coupled THM modeling capability for predicting the dynamics of fracture stimulation, fluid flow, rock deformation and heat transport in a singly integrated code. The new open-source version of the code is a completely renovated subset of the legacy one that solves the coupled thermal-hydraulic process (i.e., Darcy's flow and heat transport) in compressible fractured/un-fractured porous medium.

The novelties of this work mainly include these three aspects. First, this study has proposed a mixed-dimensional rock–fracture model, in which the fractures are represented with 2D elliptical surfaces embedded in 3D rock matrix. Unlike the 2D single fracture model used in Zeng et al. 2013, our 3D model takes into account the inter-fracture interference with respect to the fracture horizontal spacing, whose long-term impact on the production wellbore temperature cannot be neglected for a 30-year production period. Second, an exceptionally large geothermal gradient of 65°C per km depth is used in our reservoir model, according to the geothermal data measured in the Snake River Plain, Idaho (Blackwell et al. 1992). Therefore, unlike in a normal reservoir of relatively lower geothermal gradient (25~30°C per km depth), where the horizontal orientation might be optimal for a doublet well layout, this work also considers an alternative doublet well layout that has a downward well deviation angle, whose potential effect on heat production performance is exclusively analyzed in the present study. Third, compared with most existing codes that are so far either closed-source or only commercially available in this area, the newly developed open-source FALCON code has demonstrated a reservoir code development strategy with an attempt to provide an unparalleled easiness for user customization and multi-physics coupling.

The rest of this paper is organized as follows: Section 2 presents the governing equations for the coupled fluid flow and heat transport in a geothermal reservoir environment, and the constitutive models for calculating the water thermodynamic properties. Section 3 briefly describes the Galerkin FEM formulation and numerical methods implemented in the FALCON code. Section 4 introduces the set-ups of our conceptual EGS model. Section 5 reports the numerical results of the simulation test cases and sensitivity analysis. Finally, Section 6 gives concluding remarks and outlook for future work.

2. MATHEMATICAL MODEL

The mathematical models that describe the geothermal reservoir systems can be found in an abundance of literature. This section will briefly summarize the formulations in the literature for geothermal systems (Brownell et al. 1977; Faust & Mercer, 1979).

2.1 Governing Equations

A pressure-temperature (P-T) based formulation for the single-phase simulation of water-saturated systems is adopted in this work. The mass conservation for the fluid phase in the porous medium may be written as:

$$\frac{\partial(\phi\rho_{\mathrm{w}})}{\partial t}+\nabla\cdot(\rho_{\mathrm{w}}\mathbf{q})-\acute{q}_{\mathrm{w}}=0 \tag{1}$$

where ∇ is the vector differential operator, $\mathbf{q}$ the Darcy flux vector (unit: m·s^{-1}), ρ_{w} the density of water (unit: kg·m^{-3}), ϕ the porosity of the reservoir, and $\acute{q}_{\mathrm{w}}$ the mass source/sink term (unit: kg·m^{-3}·s^{-1}), respectively. When considering the momentum conservation of the system, we assume that Darcy's law is valid, and that the momentum balance for the fluid phase may be represented as:

$$\mathbf{q}=-\frac{k}{\mu_{\mathrm{w}}}(\nabla p_{\mathrm{w}}+\rho_{\mathrm{w}}g\nabla\mathrm{z}) \tag{2}$$

where k is the intrinsic permeability of reservoir (unit: m^2), μ_{w} the viscosity of water (unit: kg·m^{-1}·s^{-1}), g the acceleration due to gravity (unit: m·s^{-2}), and ∇z a vector of components (0, 0, -1) when gravity is taken to be aligned in the negative vertical direction. Combining Eq. (1) and Eq. (2) yields the following equation for liquid-phase water flow in a deformable, compressible geologic medium:

$$\frac{\partial(\phi\rho_{\mathrm{w}})}{\partial t}-\nabla\cdot\left(\frac{k}{\mu_{\mathrm{w}}}\rho_{\mathrm{w}}(\nabla p_{\mathrm{w}}+\rho_{\mathrm{w}}g\nabla\mathrm{z})\right)-\acute{q}_{\mathrm{w}}=0 \tag{3}$$

If we assume that the thermal equilibrium exists between the fluid and solid phases, the energy conservation can be described as below:

$$\frac{\partial[\phi\rho_{\mathrm{w}}c_{\mathrm{w}}+(1-\phi)\rho_{\mathrm{r}}c_{\mathrm{r}}]T}{\partial t}-\nabla\cdot(K_{\mathrm{m}}\nabla T)+\rho_{\mathrm{w}}c_{\mathrm{w}}\mathbf{q}\cdot\nabla T-\acute{Q}=0 \tag{4}$$

where c_{w} and c_{r} are the specific heat capacity of water and rock (unit: m^2·s^{-2}·K^{-1}), respectively, K_{m} the average thermal conductivity of the medium (unit: kg·m·s^{-3}·K^{-1}), and $\acute{Q}$ the energy source/sink term (unit: J/s, or kg·m^{-1}·s^{-3}). Eq. (3) and Eq. (4) serve as the governing equations for the coupled flow and heat transport in geological porous medium. Furthermore, if we assume ϕ, k, and K_{m} to be constant user-input parameters by default, Eq. (3) and Eq. (4) can be reduced to Eq. (5) and Eq. (6), respectively as below:

$$\phi\frac{\partial\rho_{\mathrm{w}}}{\partial p}\frac{\mathrm{d}p}{\mathrm{d}t}+\nabla\cdot\mathbf{q}_{\mathrm{M}}-\acute{q}_{\mathrm{w}}=0 \tag{5}$$

$$C_{\mathrm{m}}\frac{\mathrm{d}T}{\mathrm{d}t}-K_{\mathrm{m}}\nabla\cdot\nabla T+\mathbf{q}_{\mathrm{E}}\cdot\nabla T-\acute{Q}=0 \tag{6}$$

where $\rho_{\mathrm{w}}\mathbf{q}$ is replaced by $\mathbf{q}_{\mathrm{M}}$ (unit: kg·m^{-2}·s^{-1}), $\phi\rho_{\mathrm{w}}c_{\mathrm{w}}+(1-\phi)\rho_{\mathrm{r}}c_{\mathrm{r}}$ is replaced by C_{m} (unit: kg·m^{-1}·s^{-2}·K^{-1}), and $\rho_{\mathrm{w}}c_{\mathrm{w}}\mathbf{q}$ is replaced by $\mathbf{q}_{\mathrm{E}}$ (unit: kg·s^{-3}·K^{-1}), respectively, for simplicity. Eq. (5) and Eq. (6) are the default pressure-temperature based governing equations being used in the present work.

2.2 Fluid Thermodynamic Properties

In the present work, two different constitutive models are presented for the calculation of the thermodynamic properties and viscosity of the liquid-phase water:

1) Based on the IAPWS-97 formulation (Wagner et al., 2000), the water-steam equation of state (WSEOS) approach can be applied in the water, steam, and supercritical regions. In this approach, the WSEOS is used to calculate and return the phase thermodynamic properties (i.e., density, internal energy) of water and steam, based on pressure ($\leq$ 100 MPa) and temperature ($\leq$ 800° C) as input variables. Based on the density and temperature as input variables, the viscosity formula in IAPWS-97 (Cooper 2008) is then used to calculate and return the viscosity of either water or steam, depending on the input density value.

2) Alternatively, two temperature based functions can be used to calculate the liquid-phase water density and viscosity in a limited range of temperature between 0°C and 300°C (Graf 2009). Assuming the water pressure is below the critical point, the dependency of water density and viscosity on water temperature can be described in the following equations, respectively:

$$\rho_{\mathrm{w}}=1000\left[1-\frac{(T-3.9863)^2}{508929.2}\frac{T+288.9414}{T+68.12963}\right],\ \text{for}\ 0℃\leq T\leq 300℃ \tag{7}$$

$$\mu_{\mathrm{w}} = \begin{cases} 1.787 \times 10^{-3} e^{(-0.03288 + 1.962 \times 10^{-4} T)T}, \text{for } 0℃ \le T \le 40℃ \\ 10^{-3}\left(1 + 0.015512(T - 20)\right)^{-1.572}, \text{for } 40℃ < T \le 100℃ \\ 10^{-4}\left(0.2414 \times 10^{\frac{247.8}{T + 133.15}}\right), \text{for } 100℃ < T \le 300℃ \end{cases} \tag{8}$$

3. NUMERICAL METHODS AND CODE DEVELOPMENT

3.1 Galerkin Finite Element Discretization

Using the standard finite element spatial discretization, the weak forms of Eq. (5) and Eq. (6) are

$$\sum_{e}^{n_{el}} \int_{\Omega_e} \left(\frac{\mathrm{d}p}{\mathrm{d}t} \phi \frac{\partial \rho_{\mathrm{w}}}{\partial p} W_h - \mathbf{q}_{\mathrm{M}} \cdot \nabla W_h - \acute{q} W_h \right) \mathrm{d}\Omega + \int_{\Gamma} \mathbf{q}_{\mathrm{M}} \cdot \mathbf{n} W_h \, \mathrm{d}\Gamma = 0 \tag{9}$$

$$\sum_{e}^{n_{el}} \int_{\Omega_e} \left(\frac{\mathrm{d}T}{\mathrm{d}t} C_{\mathrm{m}} W_h + (K_m \nabla T - T\mathbf{q}_{\mathrm{E}}) \cdot \nabla W_h - \acute{Q} W_h \right) \mathrm{d}\Omega + \int_{\Gamma} (-K_{\mathrm{m}} \nabla T + T\mathbf{q}_{\mathrm{E}}) \cdot \mathbf{n} W_h \, \mathrm{d}\Gamma = 0 \tag{10}$$

In Eq. (9) and Eq. (10), Ω_e is the volume of element e, Γ denotes the boundary of the domain, $\mathbf{n}$ represents the unit vector normal to the boundary, and W_h is the interpolation functions in the finite element space.

3.2 Stabilization for Heat Transfer

In an energy conservation equation, e.g., Eq. (6), the element Peclet number Pe_h can be defined as:

$$Pe_h = \frac{h|\mathbf{q}_{\mathrm{E}}|_2}{2K_m} \tag{11}$$

where h is the characteristic element size. Since the K_m does not vary hugely in fractured reservoirs of different solid medium, the value of Pe_h is mainly determined by the $|\mathbf{q}_{\mathrm{E}}|_2$, which can be very high near the injection and production wellbores (e.g., 2 ~ 4 orders of magnitude higher than in the rest of the reservoir. As it has been theoretically proved, the numerical oscillations of the energy variable (i.e., temperature) will occur when $Pe_h > 1$. This is a notorious numerical downside of the standard Galerkin FEM when used to model convection-dominated problems. In the present work, the famous Streamline/Upwind Petrov Galerkin (SUPG) scheme (Hughes at al. 1986a) is adopted to achieve a stabilized formulation of Eq. (10). Following the SUPG scheme, Eq. (10) can be recast by adding an extra term in the volume integral as below,

$$\sum_{e}^{n_{el}} \int_{\Omega_e} \left(\frac{\mathrm{d}T}{\mathrm{d}t} C_{\mathrm{m}} W_h + (K_m \nabla T - T\mathbf{q}_{\mathrm{E}}) \cdot \nabla W_h - \acute{Q} W_h + \tau_1 R_E \mathbf{q}_{\mathrm{E}} \cdot \nabla W_h \right) \mathrm{d}\Omega + \int_{\Gamma} (-K_{\mathrm{m}} \nabla T + T\mathbf{q}_{\mathrm{E}}) \cdot \mathbf{n} W_h \, \mathrm{d}\Gamma = 0 \tag{12}$$

where $R_E = C_{\mathrm{m}} \frac{\mathrm{d}T}{\mathrm{d}t} - K_{\mathrm{m}} \nabla \cdot \nabla T + \mathbf{q}_{\mathrm{E}} \cdot \nabla T - \acute{Q}$ is the strong-form residual of Eq. (6); and $\tau_1 = h_{\mathrm{SUPG}}/2(|\mathbf{q}_{\mathrm{E}}|_2 + \varepsilon)$, where ε is a small number to avoid dividing by zero if $\mathbf{q}_{\mathrm{E}}$ is close to zero, and h_{SUPG} is an element characteristic length (e.g., we use the minimal nodal spacing of the element). The $K_{\mathrm{m}} \nabla \cdot \nabla T$ is equal to zero when the linear approximation polynomial solution is used. The formulation of τ_1 may vary depending on the shape of element (e.g., triangle or quadrilateral in 2D; tetrahedron, or prism, or pyramid, or hexahedron in 3D). But we did not encounter outstanding trouble by using the presented formulation in our simulations. The SUPG scheme in Eq. (12) is able to deliver stabilized and low-diffusion numerical solution of coupled flow and heat transport for smooth problems. However, it cannot eliminate the local over- and under-shoots in the energy variable solution if there exist local discontinuities or large thermal gradients, due to the absence of a control mechanism of thermal gradients in the directions other than the streamline. To the best of our knowledge, a TVD scheme does not exist for the Galerkin FEM. Nevertheless, the SUPG Discontinuity-Capturing scheme (Hughes et al 1986b), termed SUPG-DC, is adopted in this work with an attempt to remove most but not all of the local under- and over-shoots of the temperature solution. Following the SUPG-DC scheme, Eq. (12) can be further recast by adding one more extra term:

$$\sum_{e}^{n_{el}} \int_{\Omega_e} \left(\frac{\mathrm{d}T}{\mathrm{d}t} C_{\mathrm{m}} W_h + (K_m \nabla T - T\mathbf{q}_{\mathrm{E}}) \cdot \nabla W_h - \acute{Q} W_h + R_E(\tau_1 \mathbf{q}_{\mathrm{E}} + \tau_2 \mathbf{q}_{\mathrm{E}_{\|}}) \cdot \nabla W_h \right) \mathrm{d}\Omega + \int_{\Gamma} (-K_{\mathrm{m}} \nabla T + T\mathbf{q}_{\mathrm{E}}) \cdot \mathbf{n} W_h \, \mathrm{d}\Gamma = 0 \tag{13}$$

In Eq. (13), $\tau_2 = \max(0, \tau_{\|} - \tau_1)$, where the "max" function is used to guard against $\tau_{\|} - \tau_1$ becoming negative, which can occur in distorted element geometries. The rest of the two coefficients are

$$\tau_{\|} = \frac{h_{\|}}{\frac{2\mathbf{q}_{\mathrm{E}} \cdot \nabla T}{|\nabla T|_2} + \varepsilon} \tag{14}$$

$$q_{\mathbf{E}_{\|}} = \frac{\mathbf{q}_{\mathrm{E}} \cdot \nabla T}{|\nabla T|_2^2} \nabla T \tag{15}$$

where the subscript || denotes the direction of the local streamline. Our numerical experiments have shown that, the SUPG-DC scheme can work effectively if the initial discontinuity in temperature field is in the fractured reservoir. But it could lead to divergence if the initial discontinuity is on the domain boundary, for example, the injection of cool water into a hot fractured reservoir from an injection wellbore boundary surface. More advanced stabilization schemes aimed to consistently remove the local over- and under-shoots, for example, in Do Carmo & Galeão 1991, and Codina 1998, will be attempted in future.

3.3 Boundary Conditions

The three most frequently used BCs for the mass conservation in Eq. (9) include: 1) The Dirichlet pressure BC, with which a pressure value can be prescribed at either the injection/production wellbore boundaries, or far-field boundaries. 2) The Neumann mass flux BC, with which a mass flux normal to a boundary surface, $-\mathbf{q}_{\mathrm{M}} \cdot \mathbf{n}$, can be prescribed either at the injection/production wellbore boundaries, or the no-flow boundaries or symmetry plane by setting $\mathbf{q}_{\mathrm{M}} \cdot \mathbf{n} = 0$. 3) The Neumann free outflow BC, with which the $\mathbf{q}_{\mathrm{M}}$ value at a quadrature point of a boundary surface is interpolated from its host element. This BC can be used to model a free flow exit.

The three most frequently used BCs for energy conservation in Eq. (10) include: 1) The Dirichlet temperature BC, with which a temperature value can be prescribed at either the injection wellbore boundaries, or far-field boundaries. 2) The Neumann heat inflow BC, with which a heat flux normal to a boundary, $(-K_{\mathrm{m}}\nabla T + T\mathbf{q}_{\mathrm{E}}) \cdot \mathbf{n}$, can be prescribed at the injection wellbore boundary. 3) The Neumann heat outflow BC, with which the heat flux $\mathbf{q}_{\mathrm{E}}$ value at a quadrature point of a boundary surface is interpolated from its host element. This BC can be used to model the heat transport at the production wellbore boundary.

3.4 Source/Sink Terms

The source/sink terms include both the loss and/or gain of fluid mass and energy due to injection and pumping. There are two ways to represent an injection or pumping well as described below, but the best choice is upon specific applications.

1) Explicitly mesh the well bore. This approach works best for near-wellbore, small-scale models in which the injection or pumping of mass/energy can be approximated by a prescribed flux boundary (Neumann boundary). However, for reservoir-scale models, such representation will result in too many elements, and quickly become unpractical even with parallel computing. Geometric simplification for representing the wells is usually acceptable to use this approach for reservoir-scale models, when the simulation accuracy of near-wellbore phenomena is not concerned.

2) Represent the injection/pumping wells as point or line source/sink terms. This approach is also chosen often for large-scale models, since the implementation is not constrained by the complexity of geometric representation. In this approach, the injected (or pumped) fluid mass and energy is distributed to the nodes of the grid cells where the wellbore is located, and weighted by the distance between the well and the neighboring nodes by using finite element basis functions. However, this seemingly convenient approach could lead to severe numerical instability and even solution breakdown at the presence of strong flow velocity near wellbores (as discussed in Section 2.2), if no effective numerical stabilization method is applied.

3.4 Code Development

The governing equations and numerical methods described above have been implemented in the open-source geothermal reservoir simulation code, FALCON (Xia et al., 2015a). Some of the core computational capabilities include: 1) fully-coupled, fully-implicit solver, 2) dimension independent physics, 3) automatically parallel (largest runs >100,000 CPU cores), 4) modular development simplifies code reuse, 5) built-in mesh adaptivity, 6) dimension agnostic, parallel geometric search (for contact related applications), and 7) flexible, pluggable graphical user interface.

Moreover, in addition to the brief introduction of the code in Section 1.3, this subsection further presents an overview of the code in terms of design philosophy and programming architecture. The FALCON code has been developed using the open-source finite-element Multiphysics Object-Oriented Simulation Environment (MOOSE) framework (Gaston et al., 2009), which has a layered structure, as shown in Figure 1. The lower layer interfaces with several open-source libraries. In particular, the libMesh finite element framework (Kirk et al., 2006) provides a core set of parallel finite-element libraries. Coupled with interfaces to linear and nonlinear solvers from both PETSc (Balay et al. 2014) and Trilinos (Heroux et al. 2005), MOOSE and application codes developed upon it provide considerable flexibility including the abilities to swap out solver libraries and to utilize diverse large scale parallel computing resources. The middle layer of MOOSE provides a set of core functionalities necessary for the residual and Jacobian (more precisely, the preconditioner) evaluations required by a physics-based preconditioning, strongly convergent nonlinear solver such as the preconditioned Jacobian-Free Newton-Krylov (JFNK) algorithm, and an efficient linear solvers such the as the generalized minimal residual (GMRES) algorithm (Knoll et al. 2004), for fetching the designated test and shape functions, numerical integration using Gaussian quadrature, and coupling physics. The top layer of MOOSE, referred to as the kernel, is the interface with physics where the FALCON code is built. It is convenient to think of a kernel as a piece of the residual term in the weak forms of PDEs, for example, the diffusion term, advection term, time derivative term in Eq. (10) (see Appendix A for a list of kernels in the FALCON code). Kernels may be coupled together to achieve different application goals. All kernels are required to supply a residual, which usually involves summing products of finite element shape functions. Kernels may also provide diagonal and off-diagonal blocks of the (approximate) Jacobian matrix for the purpose of building certain preconditioners. Indeed, the adoption of the "kernels" concept from the underlying MOOSE framework has made FALCON highly extensible and flexible in terms of the virtual abstract physics and transport interfaces. In addition to the code design and development, the developed capabilities in the FALCON code have undergone a critical verification and validation (V&V) process (Xia et al. 2015b). Numerical results obtained by the code agree well with either the available analytical solutions or experimental data, indicating the verified and validated implementation of these capabilities in the code.

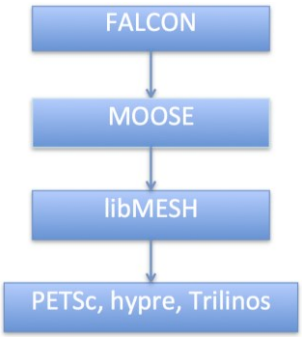

Figure 1: Hierarchical framework used to build the FALCON code based on the MOOSE library.

4. THE CONCEPTUAL MODEL

4.1 Fractured Reservoir

The characteristics of a multi-dimensional fractured reservoir network, such as the permeability, aperture and fracture geometric shapes, may be subject to change during the heat production process of an EGS. Modeling the coupled THM processes in the fractured reservoir normally requires an explicit description of fracture distribution that resolves many aspects of the rock physics, for example, variations of fracture aperture with respect to local effective stress, rock deformations due to shear failure, and constitutive relationships between the fracture aperture and fracture thermal conductivity as well as thermo-elasticity. Modeling the coupled THM processes instead of TH may result in a much more accurate but also significantly more complex EGS model for the heat production process. Nevertheless, according to a numerical study on the impacts of different coupled processes (e.g., hydro-mechanical and thermo-mechanical) on the EGS heat production performance (McDermott et al. 2006), the energy production rate is minimum when the fluid properties in the fractured reservoir are functions of only the fluid pressure and temperature while the rock mechanical properties are kept constant, that is, without considering the hydroelastic or thermoelastic interactions between the rock and fluid. Hence, a lower limit of the EGS thermal energy production rate may be estimated in the case that the physical properties of rock are constant in the system. Therefore, in our conceptual EGS reservoir model, we can reasonably assume that after the man-made fractures have been created by stimulation, the mechanical properties of the fractured reservoir remain unchanged during the period of heat production process. Furthermore, our reservoir model is assumed to be a dual-porosity/dual-permeability system, that is, un-fractured rock matrix blocks separated by fractures, and the matrix blocks and fractured reservoirs are assumed to be slightly compressible homogeneous porous medium, in which the coupled fluid flow and heat transport processes may be represented by Eq. (5) and Eq. (6). Indeed, these practical assumptions had been adopted in many recent studies, for example, see Sanyal et al. 2005, Jiang et al. 2014, Bujakowski et al. 2015, and Chen at al. 2016.

4.2 Well Layout

As it has been extensively evaluated, the well drilling process is a very expensive in terms of both capital investment and work hours (for example, see Barbier 2002, and Polsky et al. 2008). Thus before the actual well drilling, a well layout design involving a cycle of design, assessment and redesign, is absolutely needed until an optimal design is reached. Figure 2a illustrates the symmetry plane of one of our 3D conceptual EGS reservoir models, where a pair of horizontal doublet wells is connected by a set of vertically extended single large wing fracture planes. Since the potential geotechnical stimulation strategies to create this kind of single large wing fractures had been discussed in Jung 2013, we do not attempt to discuss it here. In each of the fracture planes, the vertical distance between the injection and production wellbores is denoted by d_{v}, and the horizontal spacing between each two neighboring fracture planes is denoted by d_{h}. The fracture planes are enumerated from #1 to #5 along the positive x-direction. We chose the midpoint of the #1 fracture plane to be the reference depth below the ground surface, and denote its vertical coordinate by z_{ref}. Moreover, based on the assumption that a large geothermal gradient of 65°C per km depth exists in our imaginary subsurface domain, we specify a reasonable reference fracture depth of $z_{\mathrm{ref}} = -3000\mathrm{m}$, and accordingly a reference temperature of 220°C at this depth, and a reference pressure of 30 MPa at the #1 production wellbore.

In addition to the regular horizontal well layout in Figure 2a, an alternative doublet wells layout with a downward deviation angle of $\alpha = 45°$ is also considered, as shown in Figure 2b. This deviated well layout is potentially a feasible well drilling strategy to reach a greater depth instead of a straightforward vertical well drilling that might be significantly more difficult or even impossible, because of the prohibitive stress condition along the vertical direction. In order to make a relatively fair performance comparison between the two scenarios, the d_{v} and d_{h} are kept identical between the two scenarios. Based on part of the metrics suggested in Jung 2013 (i.e., an industrial production-level EGS should consist of 30~40 equidistant fractures connecting two 1km long parallel well sections with a well separation of about 500m), we specify $d_{\mathrm{v}} = 500\mathrm{m}$ in the two scenarios. However, since the computational costs (e.g., computing time and storage) for modeling 30~40 fractures in 3D would be very expensive even for supercomputers, we have chosen only five of such fractures in this study. Nevertheless, we believe that the reduced-scale models in our study are 1) sufficient to reveal the sensitivity of long-term heat production performance upon some design constraint factors, such as fracture spacing, flow rate, and well orientation, and 2) scalable to estimate the performance of a full-scale model.

To complete the water circulation and heat production processes, an injection pump that connects the injection well and a suction pump that connects the production well are installed on the ground. The water injection rate at the injection wellbores is kept constant (e.g., 3.14 kg/s into each fracture plane in our reference test case), while the suction pump draws the heated water out of the reservoir through

the production well, and pumps the water into a binary cycle power plant. The outflow from the power plant is cooled down to about 80°C, and re-injected into the fractured reservoir via the injection well.

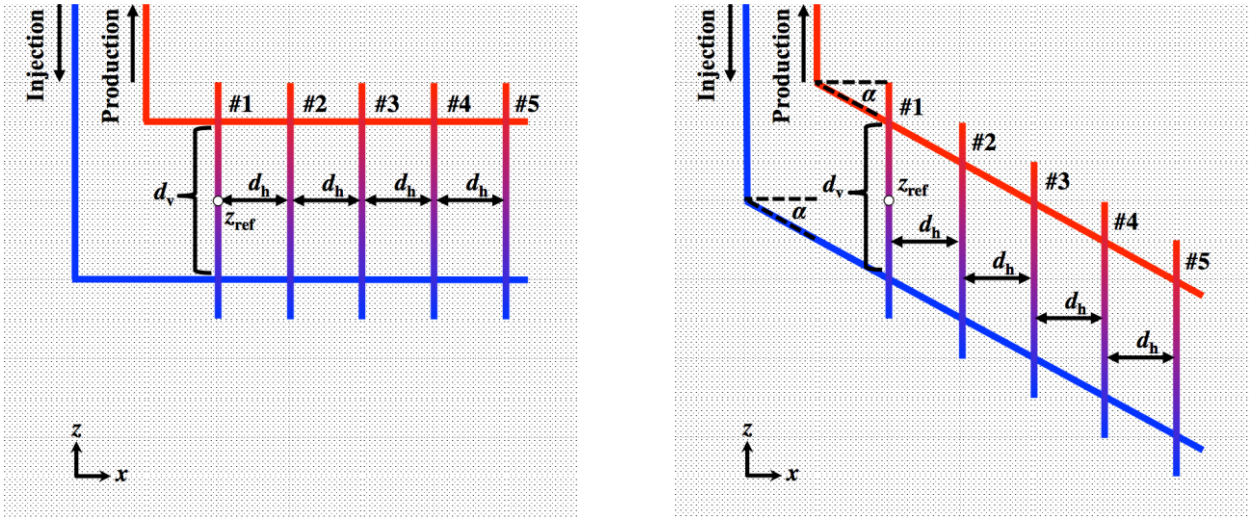

(a) (b)

Figure 2: Illustrations of the well orientation: (a) horizontal, (b) with a downward deviating angle of α.

4.3 Geometric Configuration, Domain Discretization, and Material Properties

Figure 3 illustrates the two steps to create the geometric configuration and finite element mesh for our hypothetical geological system: 1) creation of a 2D domain and mesh, and 2) creation of a mixed-dimensional 2d-fracture/3d-matrix system. The CUBIT toolkit (Blacker et al. 1994) is used for the geometry/mesh creation to be described below. Due to the symmetric nature of our model, only half of the system domain needs to be modeled.

For the first, a 2D planar fracture-matrix system is created in the *y*-*z* plane with the *x*-coordinate equal to zero, where the fracture plane (red color) is represented by a semielliptical disk with a primary radius of 750m in the vertical *z*-direction and secondary radius of 500m in the horizontal *y*-direction. As shown in Figure 3a, the fracture is encompassed by the rock matrix (grey color) whose outer boundary is represented by a semicircular curve with a radius of 1000m. Due to the absence of actual field data for such a single large fracture, its shape and size are thus chosen hypothetically, but reasonably enough to indicate the directions of the minimum and maximum stresses when subjected to the initial stimulation process. Moreover, since we are not interested in the flow behaviors close to the wellbores, the fluid injection and pumping in the reservoir is modeled using two semicircular boundary curves with a relatively large radius of 2m, and aligned vertically with a vertical distance of $d_v = 500$m. The resulting 2D domain is then discretized using the unstructured quadrilateral elements, where most of the elements are clustered near the injection and production boundaries. As mentioned in Section 3.4, this simplification of wellbore geometries will substantially help reduce the total elements of the mesh, and improve the efficiency of solving. Somehow it should not confused that the physical quantities to be simulated at the injection and production boundaries, such as the fluid pressure and temperature, only represent their values in the near-wellbore regions, but not right at the wellbores.

For the second, the 2D planar domain is first extruded in *x*-direction for a total horizontal length equal to $4d_h + 2d_{ex}$, with an optional downward deviating angle, α (= 0° or 45°), as shown in Figure 3b. The resulting 3D block domain is then cut split for five times by a plane normal to the *x*-direction at locations $x = d_{ex}$ (tagged #1), $d_{ex} + d_h$ (tagged #2), $d_{ex} + 2d_h$ (tagged #3), $d_{ex} + 3d_h$ (tagged #4), and $d_{ex} + 4d_h$ (tagged #5), respectively, as shown in Figure 3c. Thanks to the mixed-dimensional finite-element modeling capability inherited from the underlying MOOSE framework, the FALCON code allows the five zero-thickness semielliptical planes resulted from the cuts to be used for representing the fracture planes imbedded in the 3D block. It was shown in a similar work by Reichenberger et al. 2006, the use of lower-dimensional fractures in a higher-dimensional reservoir could not only reduce the computational costs, but also improve the efficiency of the implicit solver. The d_{ex} is the extra horizontal space beyond the first and last fracture planes, and it has to be wide enough so as not to let the cooling fronts reach the far-field boundary at the end of simulations. Finally, the resulting sub-blocks are meshed with the unstructured hexahedral elements extruded from the existing quadrilateral elements, at a fixed element interval of 10m within the inter-fracture horizontal spacing, d_h (d_h= 30m or 50m) and 15m within the extra space, d_{ex} (d_{ex} = 60m). Thus in the present work, a 3D mesh with any combination of d_h and α will have the same total number of elements (111,160) and points (118,570).

Proper boundary conditions (BCs) are required for the coupled fluid flow and heat transport to be simulated on the generated meshes. For the mass conservation of fluid flow, a constant mass flow rate, q'_w is imposed at all of the injection boundaries, while a constant reference fluid pressure of 30 MPa is prescribed at the production boundary of fracture #1, as the horizontal production well is assumed to locate about 3000m below the ground surface. The no-flow/no-penetration condition (i.e., zero pressure gradient) is imposed on the symmetry *y*-*z* plane and far-field boundary. In the present study, the gravitational force can be neglected, since it is a minor resisting force compared with the injection fluid pressure in the field. For the energy conservation of heat transport, a temperature of 80°C is

fixed at all of the injection boundaries, while the energy outflow condition are set at the production boundaries. The adiabatic condition (i.e., zero temperature gradient) is imposed on the symmetry *y*-*z* plane and far-field boundary.

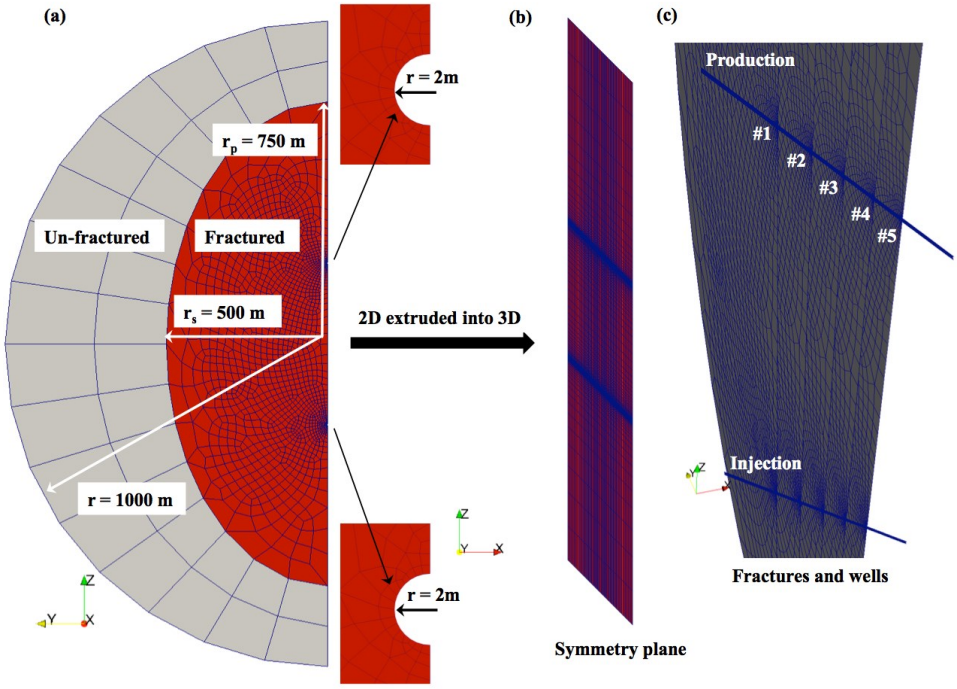

Figure 3: The mixed-dimensional geometric configurations and meshes of the EGS model used for simulations: (a) the initial 2D geometry; (b) the extrusion from 2D to 3D along the direction of wells; (c) the five 2D planar fractures.

The material properties of the dual-porosity/dual-permeability system for our conceptual EGS reservoir model are summarized in Table 1, where both the 2D fractured reservoir planes and the 3D un-fractured rock matrix blocks are considered as fully-saturated homogeneous porous medium with their own physical properties. However, unlike some prior research works in which the sensitivities of the key reservoir material properties such as reservoir permeability and thermal conductivity were evaluated in a detailed manner (e.g., see Zeng et al. 2013a and Zeng et al. 2013b), the present work only adopts one set of typical property values within their observed ranges according to the actual field data of the Snake River Plain in Idaho (Blackwell et al. 1992). We acknowledge that those properties may have a huge impact on the lifespan of the EGS heat production, and are hence worth being carefully assessed for a specific EGS reservoir site. For example, a high fracture permeability may lead to the unwanted early thermal breakthrough; and a high thermal conductivity of the un-fractured rock matrix may result in accelerated cool-down of the produced fluid temperature at the late production stages, owing to the thermal interference between the neighboring fractures. Although those sensitivity studies of the material properties are straightforward to conduct in our conceptual model, we believe that they are more practically meaningful when considered based on an actual reservoir fracture network instead of a hypothetical one.

Table 1: Simulation settings used in the test cases

Parameters	*Values*
Density of the rock	2700 kg/m^3
Density of the fluid	Computed from IAPWS-97
Viscosity of the fluid	Computed from IAPWS-97
Permeability of the matrix zone	1.0×10^{-20} m^2
Permeability of the fractured zone	0.5×10^{-12} m^2
Porosity of the matrix zone	0.01
Porosity of the fractured zone	0.1
Specific heat capacity of the matrix zone	790 J/(kg·K)
Specific heat capacity of the fluid	4818 J/(kg·K)
Medium average thermal conductivity of the matrix zone	3.0 W/(m·K)
Medium average thermal conductivity of the fractured zone	1.5 W/(m·K)

4.4 Initial Conditions

Proper initial conditions are necessary in order to overcome the possible start-up difficulty for simulating a fully-coupled fluid flow and heat transport process, where the temporal scale of the temperature field variation is often orders of magnitude lower than that of the pressure field variation. Thus in this work, a steady simulation is first conducted for the mass conservation equation of fluid flow with the constant thermodynamic properties of the fluid at the average reservoir conditions, in order to obtain an initial pressure solution in the field. Secondly, an unsteady simulation is started for the coupled fluid flow and heat transport, where the initial pressure distribution is taken from the result of the first simulation. A linear distribution of the initial temperature along the z-direction is specified in the filed based on the reference depth of $z_{\text{ref}} = 3000$m, and a geothermal gradient of gradient of 65°C per km of depth measured from the Snake River Plain in Idaho. As a result, the initial temperature at $z = z_{\text{ref}}$ is set to 220°, and the temperature difference between the injection and production boundaries in each fracture plane is 32.5°. Note that though the mean geothermal gradient is 25~30°C per km of depth near the surface in most of the world due to the flow of heat from within the earth (Banks 2012), there are also several other areas like Idaho's Snake River Plain in the United States, where the geothermal gradient is considerably greater (Conti et al. 2011).

5 NUMERICAL RESULTS

With the main objective to assess the sensitivity of some primary design constraints, four test cases are designed using combinations of these three parameters: 1) the fracture horizontal spacing, d_h, 2) the downward deviating angle of the horizontal wells, α, and 3) the production mass flow rate per fracture, q'_{w}, as listed in Table 2.Also as mentioned in Section 4.3, most of the physical properties of the water and rock are kept constant, while the density and viscosity of the water is calculated based on to the IAPWS-97 formulation. By doing so, it allows us to focus on the interplay of the parameters being assessed.

According to the three geometric scenarios in Table 2, three meshes are generated and used for simulations, respectively. The injection of cool water is started at time = 0, and terminated at time = 30 years. An initial time-step size, Δt = 10s, is specified for all the test cases, which has to be a small value initially because of the large local element Peclet numbers of the convection-dominated heat transport near the injection boundaries. An adaptive algorithm for Δt is employed for the time stepping, in which a maximum allowable Δt is calculated in each time step. As shown in Figure 4, the Δt's are gradually increased from seconds to days, weeks, and months, as the cooling fronts are propagated further into the reservoir, and became more diffused. It is interesting to note that the average Δt in the case of ($d_h = 50$m, $\alpha = 0°$, q'_{w} = 3.14kg/s) is the largest out of the four, mainly because the use of $d_h = 50$ minimizes the inter-fracture interference. Meanwhile, as it is also constrained by the doubled flow rate, the average Δt in the case of ($d_h = 30$m, $\alpha = 45°$, q'_{w} = 6.28kg/s) is much smaller than in the other three cases. Nevertheless, those time histories of Δt's have demonstrated the superior efficiency of the implicit solver in the FALCON code.

Table 2: Configuration parameters used in the four simulations.

Test Case	*Fracture horizontal spacing, d_h (m)*	*Well deviating angle, α*	*Mass flow rate per fracture, q'_{w} (kg/s)*
1	30	0°	3.14
2	50	0°	3.14
3	30	45°	3.14
4	30	45°	6.28

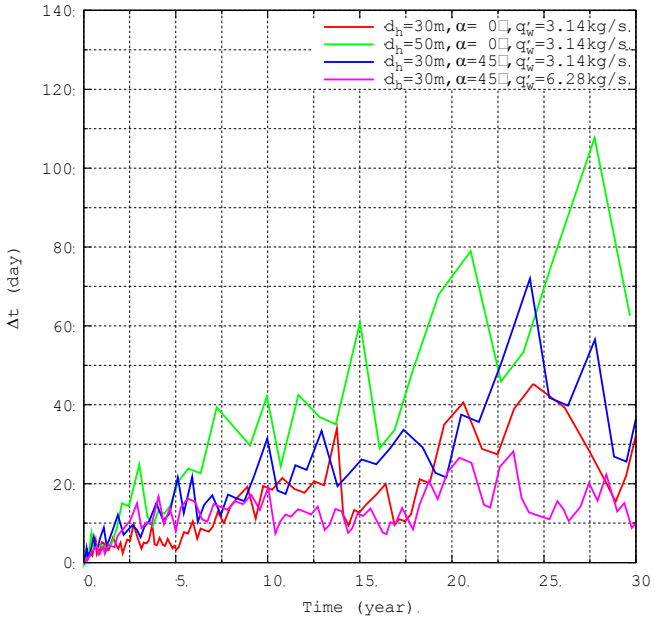

Figure 4: Time histories of the time-step sizes used in the simulation test cases.

5.1 The Example Case

In this subsection, we choose Test Case 1 (i.e., $d_h = 30$m, $\alpha = 0°$, $q'_w = 3.14$kg/s) as an example for assessing some of the resulting performance metrics of the presented conceptual EGS model.

5.1.1 Production Temperature and Thermal Energy Production Rate

For each fracture (i.e., #1, #2, #3, #4, and #5), the thermal energy production rate, Q_{pro} (J/s), can be calculated using the following area integral equation at the production boundary:

$$Q_{pro} = \int_{A_b} (T_{pro} - T_{inj}) \mathbf{q}_E \cdot \mathbf{n} \, d\Gamma \tag{16}$$

where T_{inj} is the temperature of the injected fluid, T_{pro} the temperature of the produced fluid that changes with time. In the present study, we assume that no further electricity power can be produced when T_{pro} drops down below 160°C. If we suppose only a fraction of the produced thermal energy extracted at the reservoir production boundary can be converted into the useful electric power through a binary plant, and further on, a fraction of the resulting useful electric power can be transmitted to the end consumers, the final effective electric power rate, Q_{eff}, can be approximated as follows,

$$Q_{eff} = c_{eff} Q_{pro} \tag{17}$$

where c_{eff} is an approximate ratio of conversion efficiency, and a modest value of c_{eff} = 10% is assumed in the present study. Figure 5a-b show the time histories of T_{pro} at the five production boundaries, and their corresponding Q_{eff}, respectively, over a 30-year production period. The whole heat production process can be divided into two stages: 1) a stable stage, and 2) a declining stage. At the beginning of the first stage, T_{pro} keeps increasing from its initial value of 203.75°C until it reaches 212°C after about 7 years, and gradually drops down to 203.75°C at the end of the 13th year since the production is started. The initial increase of T_{pro} is mainly due to the geothermal gradient in the reservoir, where the fluid hotter than at the production wellbore is being pumped. Accordingly, Q_{eff} maintains above 0.165 MW per fracture at the same time, experiencing an increase at first, and then a decline back to its initial rate. Thus in the first stage, the thermal energy production stays above its initial rate, and output electricity power can be steadily transmitted. However, in the second stage, T_{pro} declines from 203.75°C since the 14th year and finally to 176 ~ 188°C at different production boundaries at the 30th year. Correspondingly, Q_{eff} continues to drop from 0.165 MW to 0.125~0.14 MW per fracture, dropping by 12.7%~22.4%. Note that in the late period of the second stage, the increasing difference of Q_{eff} between the fractures is mainly due to the fracture horizontal spacing, which is not wide enough to avoid the inter-fracture interference. Above all, the reservoir temperature near the production wellbores is decreasing significantly during the second stage, and the thermal energy in the reservoir is also remarkably decaying, resulting in a continuous dropping of Q_{eff}.

According to the suggested reference metrics of an industrial production-scale EGS, a doublet-well layout connected by large single wing fractures should consist of 30~40 equidistant fractures connecting two 1km long parallel well sections with a well separation of about 500m; and a system of these dimensions should operate for at least 25 years at a flow rate of 0.1 m^3/s, and an electric power output between 5 and 10 MW and pumping power of less than 1 MW (Jung 2013). Correspondingly, if we perform an up-scaling calculation based on the least performing fracture #3, an average Q_{eff} of about 5.6 MW can be obtained with 40 of such fractures for a 30-year production period, indicating the acceptable performance of our conceptual EGS model. While there is not a consensus on the standards of those performance metrics, some other set of reference metrics can also be considered (e.g., see Evans 2010). Moreover, it is worth noting that the no-flow/no-penetration and adiabatic BCs are prescribed at the far-field boundaries of our reservoir domain. However, the thermal conduction from the surrounding rock is ever-present, especially the terrestrial heat flux from the earth crust. Therefore the actual stable stage could last longer than 13 years, and the actual production temperature during the decline stage would be higher than the presented simulation results. As a result of these factors, the actual Q_{eff} would be higher too. In addition, according to the findings in McDermott et al. 2006, the thermal energy production rate could be further improved if the rock deformation due to thermo-elasticity is considered. Above all, the presented conceptual EGS model can be regarded as a good one in terms of energy production rate.

5.1.2 Spatial Temperature Distribution

Figure 6 shows the evolution of low-temperature regions in the reservoir over the 30-year production period, where the low-temperature regions are highlighted using the solid volume with the lower and upper threshold values to be 80°C and 160°C, respectively, indicating the inability of these regions to further produce effective thermal energy. Since the production begins, the low-temperature region in each fracture plane grows gradually from the injection boundaries in an annular shape (Figure 6b-c). During the first 13 years of stable production, the annular low-temperature regions enlarge steadily, except when the cooling fronts reach the lower end of the fracture-matrix interface. Meanwhile, the thermal energy near the injection wells are extracted first, and the temperature around the production wells remains above 203.75°C. From the 14th year on, the outer boundaries of the low-temperature regions begin to bulge out toward the production wellbores (Figure 6e-f). Consequently, the temperature near the production wellbores starts to decline below 203.75°C, and the thermal energy near the production wells is being extracted, which marks the beginning of the decline stage.

5.2 Sensitivity Analysis of Design Constraints on Heat Production

Besides the presented results of test case 1, the time histories of T_{pro} and Q_{eff}, and the evolution of low-temperature regions for the other three test cases listed in Table 2 are shown in Figure 5 - Figure 10. With the results obtained from these four test cases, it is now possible to consider the sensitivity of heat production in our conceptual EGS model to the following design constraints and parameters: 1)

fracture horizontal spacing, d_h; 2) downward deviating angle of the horizontal wells, α; and 3) production mass flow rate per fracture, q'_w. It is important to note the #3 fracture is the least performing one at the end of the 30-year period in each test case. Thus we choose the results obtained from those #3 fractures as baseline production metrics per fracture for the comparative studies as follows.

5.2.1 Sensitivity to d_h

The sensitivity of heat production to d_h can be assessed by increasing d_h from 30m to 50m, while keeping $\alpha = 0°$ and q'_w = 3.14kg/s as constant between Case 1 and 2. Figure 13a-d show the dependence of T_{pro}, P_{inj}, Q_{eff}, and cumulative electric power production, $\sum Q_{eff}\Delta t$, on d_h, respectively, where Q_{eff} and $\sum Q_{eff}\Delta t$ are multiplied by an upscale factor of 40 to measure the performance of a full-scale model containing 40 of such fractures. The stable production stage during which T_{pro} stays above the initial 203.75°C in Case 2 is about 16 years, which is 3 years longer than that in Case 1 (Figure 13a). Noticeably, T_{pro} reaches the peak value of 212°C in both cases at the 7th year, but declines faster in Case 1 since the 8th year, because of the earlier occurrence of inter-fracture interference (Figure 6d). In comparison, inter-fracture interference in Case 2 is much weaker, as T_{pro} in the #3 fracture is only 4°C lower than that in the best performing fracture at the 30th year (Figure 7a), whereas it is 11.5°C in Case 1. This leads to a difference in $\sum Q_{eff}\Delta t$ by 125×10^6 kWh over the 30-year period (Figure 13d). Besides, the total increase of P_{inj} is 25% lower in Case 2 than that in Case 1 (Figure 6b), indicating the slightly lower impedance for water reinjection and thus higher system efficiency. Above all, d_h has been demonstrated as an important design constraint in our conceptual EGS model. A larger d_h means less inter-fracture interference that accelerates the decline of T_{pro}, but meanwhile it requires substantially more capital investment and work hours for the horizontal well drilling process, as noted in Section 4.2. Besides, the choice of d_h may be also subject to many other constraints, such as the possible total length of the horizontal wells size (for example, it will be more than 2km if d_h = 50m for a full-scale model that contains 40 fractures), and the rock stress distributions. In conclusion, d_h has profound impact on the long-term performance of heat production, and the optimal d_h for an EGS project should be estimated considering both the extra profit by increasing d_h and the additional costs in investment.

5.2.2 Sensitivity to α

The sensitivity of heat production to α can be assessed by changing α from 0° to 45°, while keeping $d_h = 30$m and q'_w = 3.14kg/s as constant between Case 1 and 3. Figure 14a-d show the dependence of T_{pro}, P_{inj}, Q_{eff}, and $\sum Q_{eff}\Delta t$, on α, respectively. Again, Q_{eff} and $\sum Q_{eff}\Delta t$ are both upscaled by a multiplier of 40 to indicate the performance of a full-scale model that contains 40 of such fractures. It is worth noting that we ignored the varying depths of the 40 fractures for upscaling Case 3, which means an under-prediction of the total thermal energy to extract than the actual case. Nevertheless, Case 3 can be regarded as a conservative estimation for the effect of α. In Case 3, T_{pro} is initially 7.8°C higher than that of Case 1, owing to the lower position of the #3 production boundary in this case (Figure 14a). But the evolution of T_{pro} in Case 3 follows a pattern similar to that in Case 1, along with the Q_{eff} modestly improved by 0.2~0.6 MW (Figure 14c). The initial P_{inj} in Case 3 is higher than that in Case 1 also because of the depth of the wellbores, but the increment of P_{inj} does not diff much between the two cases (Figure 14b). The reason to make such a comparison lies in the assumption that the initial vertical drill may not be able to reach as deep as 3km below ground surface for the creation of horizontal wells in Case 1. The major challenge for drilling deep boreholes is to overcome the increasing rock stress along the vertical direction. Indeed, it is quite common that the vertical wells cannot be drilled deep enough to reach the desirable temperature, despite the state-of-the-art drilling techniques. As a result, an alternative drilling approach such like the Case 3 may help effectively avoid dealing with the maximum rock stress at a reasonably higher extra cost, and reach the desirable depth for production. The benefit in terms of thermal energy production may be measured such as comparing Case 3 with Case 1. Overall, α has been observed as another primary design constraint. But the question of whether or not to choose a non-zero α, or even a changing α at different depths, varies from case to case. Sufficient data of the reservoir stress distribution needs to be obtained to aid the determination of a proper α.

5.2.3 Sensitivity to q'_w

The sensitivity of heat production to q'_w can be assessed by raising q'_w from 3.14kg/s to 6.28kg/s, while keep $d_h = 30$m and $\alpha = 45°$ as constant between Case 3 and 4. Figure 15a-d show the dependence of T_{pro}, P_{inj}, Q_{eff}, and $\sum Q_{eff}\Delta t$, on q'_w, respectively. In Case 2, the stable production stage can only last for 5 years, due to the doubled flow rate of q'_w = 6.28kg/s; since the 6th year, T_{pro} declines quickly below the initial value, and the production life comes to the end as early as at the 17th year (Figure 15c). Meanwhile, the increment of P_{inj} in Case 4 is over four times higher than that in Case 3 (Figure 15b), indicating a substantial increase of power required for water reinjection. Therefore, despite the doubled Q_{eff} in the Case 4, the overly shortened stable production stage may overshadow the gross productivity of our conceptual EGS model. Above all, q'_w has been showed as a very most important parameter for heat production. Clearly enough, a higher q'_w means a higher Q_{eff} for early stages, but it can also result in a greatly shortened stable stage and whole lifespan if q'_w is too high. In addition, a long-lasting stable level of Q_{eff} is more preferable for operation and management of the power plant. When q'_w is under a reasonable condition, there will be sufficient time for the hot fractured reservoir to heat the circulating water, and thus T_{pro} may stay at or above the initial level over the whole production period. Moreover, a lower q'_w also means a lower P_{inj} and hence lower impedance for water reinjection that consumes less power. In conclusion, the choice of q'_w has an significantly effect on the output electric power rate and production lifespan; the optimal q'_w for an actual EGS project should be determined based on the desired Q_{eff} and production lifetime, as well as the cost of power for reinjection & pumping.

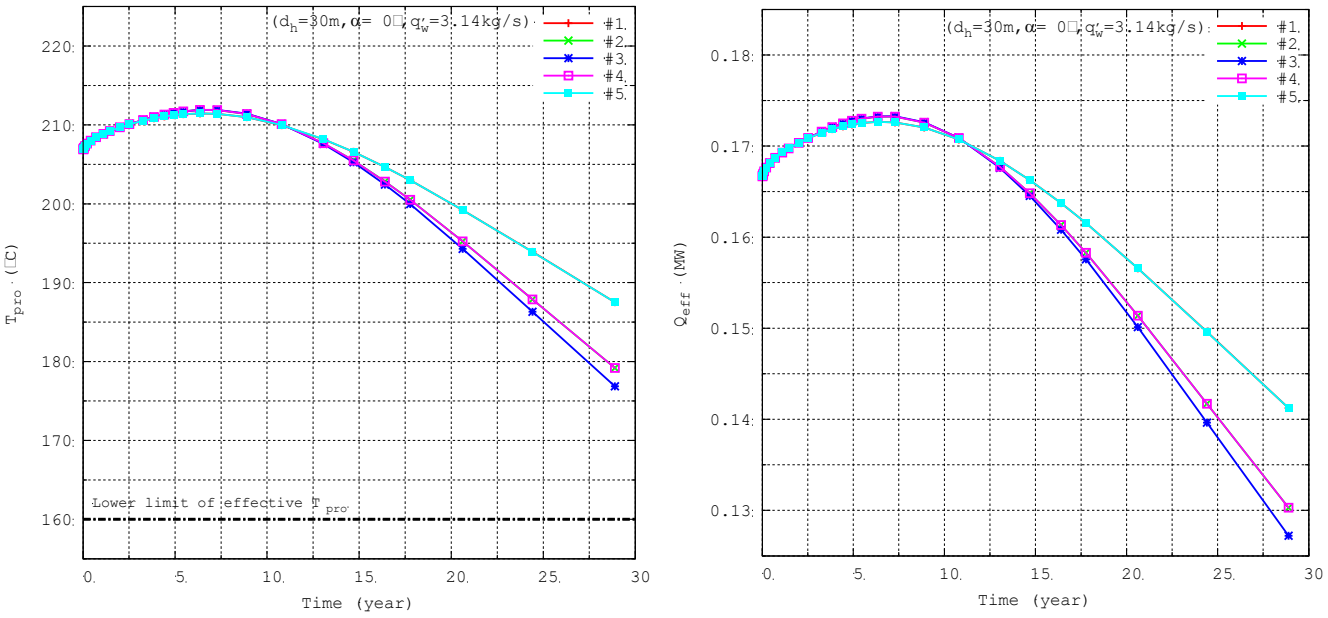

(a) (b)

Figure 5: Time histories of (a) the produced fluid temperature from the five production boundaries, and (b) the corresponding useful electric power rates ($d_h = 30$m, $\alpha = 0°$, q'_w =3.14kg/s).

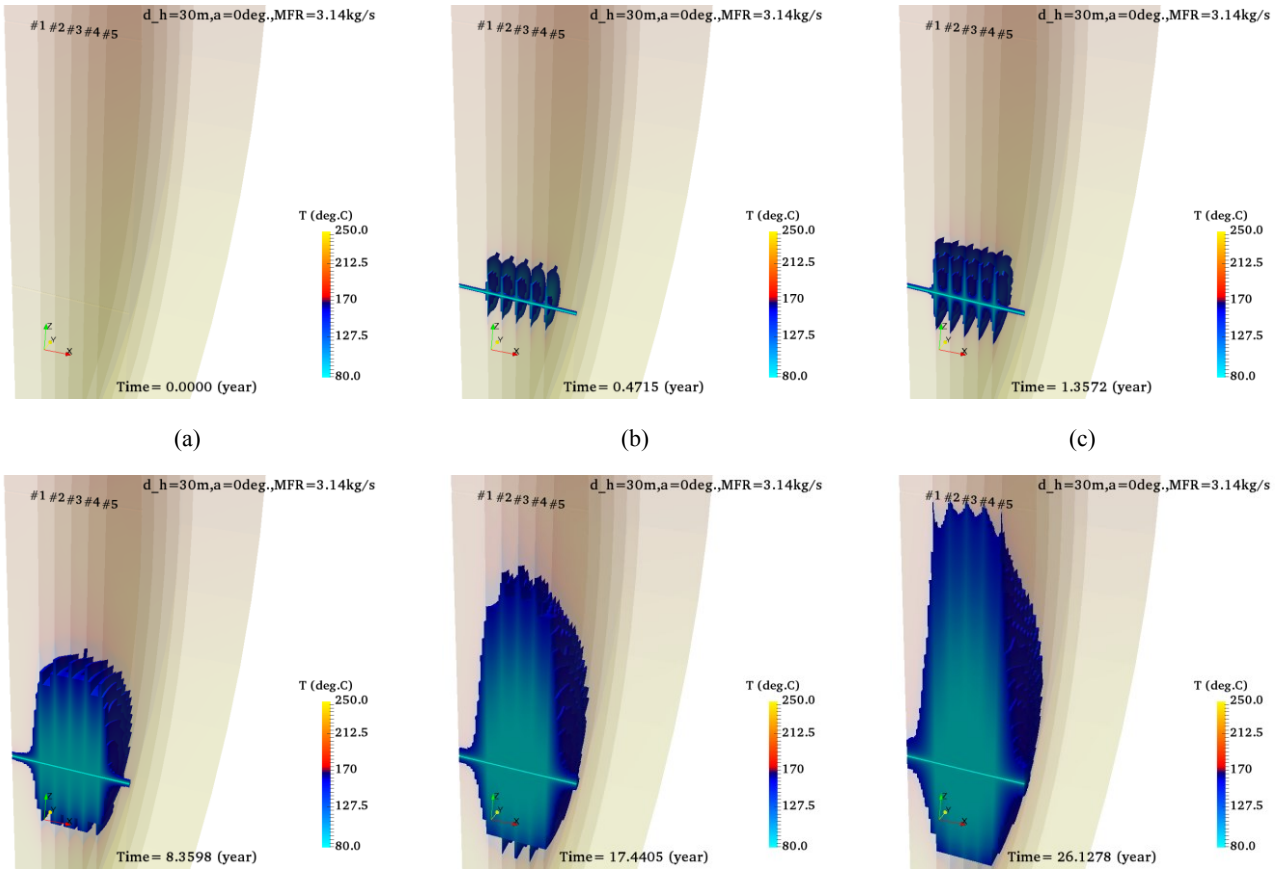

(a) (b) (c)

(d) (e) (f)

Figure 6: Evolution of the low-temperature regions in the reservoir ($d_h = 30$m, $\alpha = 0°$, q'_w=3.14kg/s).

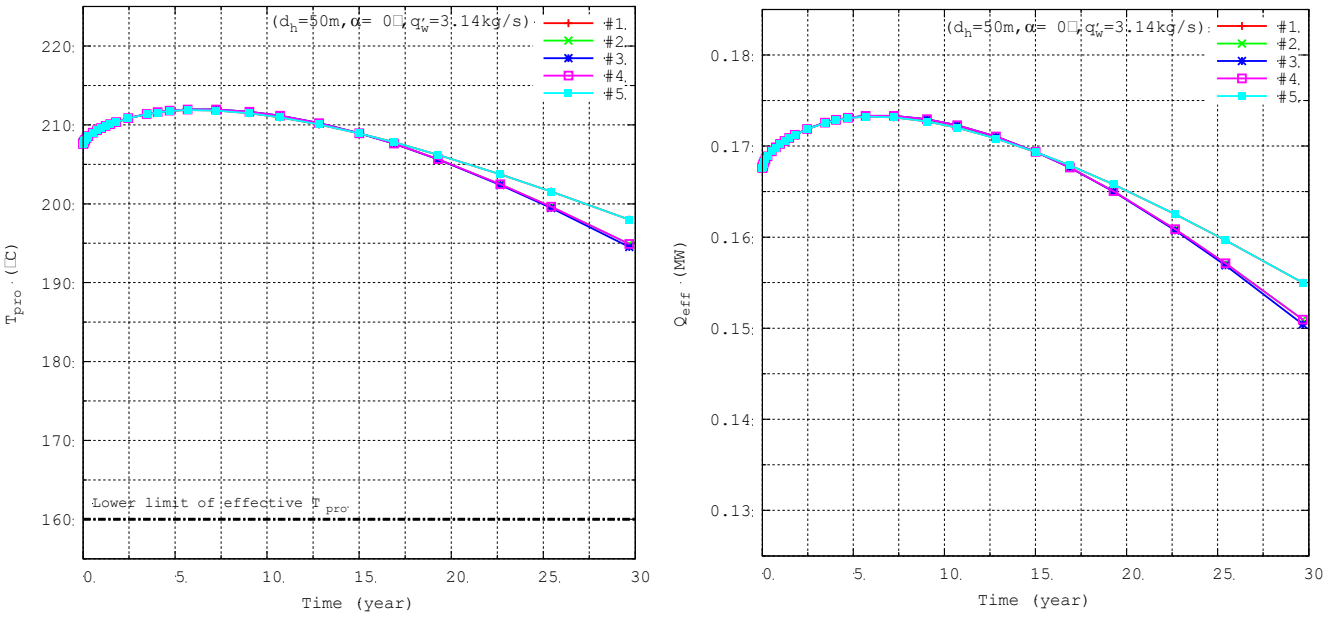

(a) (b)

Figure 7: Time histories of (a) the produced fluid temperature from the five production boundaries, and (b) the corresponding useful electric power rates ($d_h = 50$m, $\alpha = 0°$, q'_w=3.14kg/s).

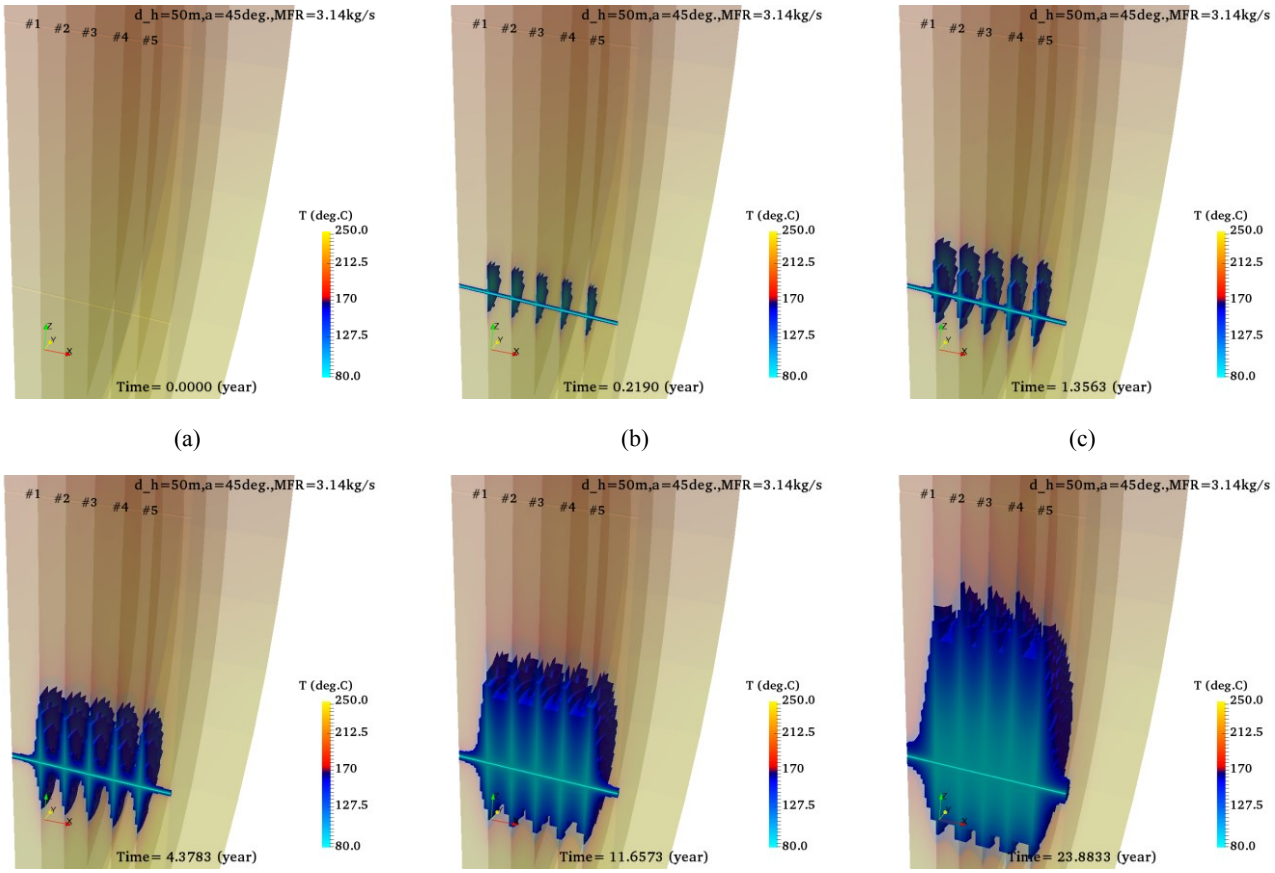

(a) (b) (c)

(d) (e) (f)

Figure 8: Evolution of the low-temperature regions in the reservoir ($d_h = 50$m, $\alpha = 0°$, q'_w=3.14kg/s).

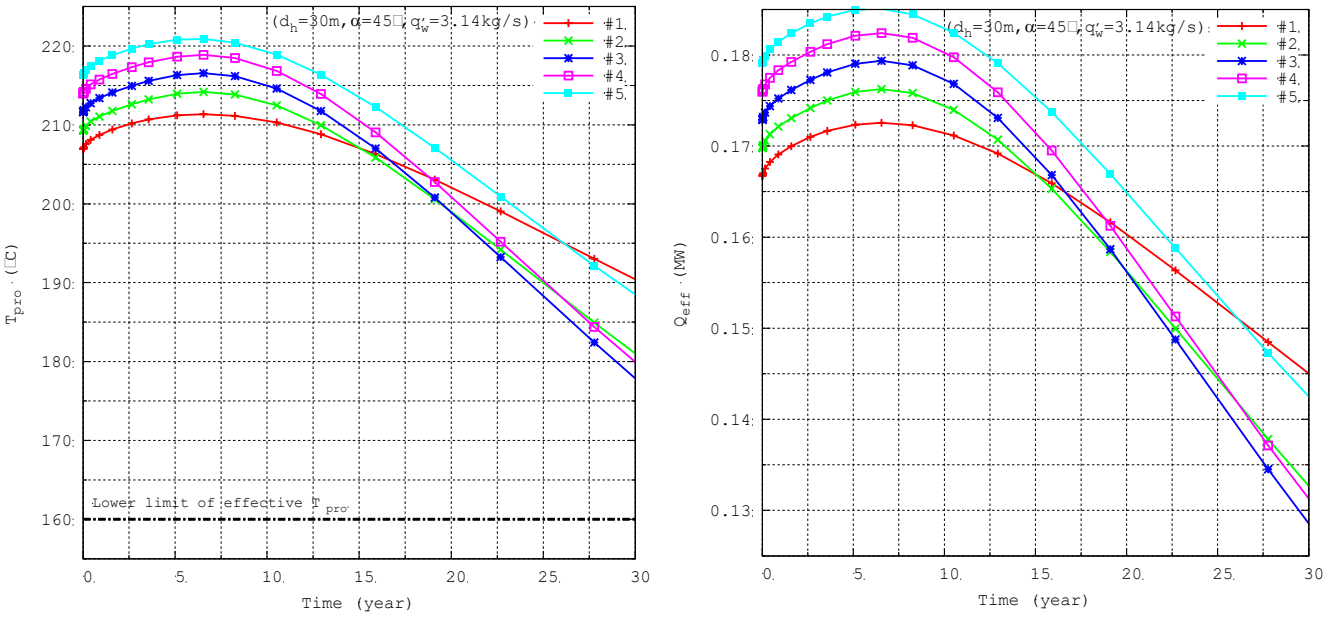

(a) (b)

Figure 9: Time histories of (a) the produced fluid temperature from the five production boundaries, and (b) the corresponding useful electric power rates ($d_h = 30$m, $\alpha = 45°$, q'_w=3.14kg/s).

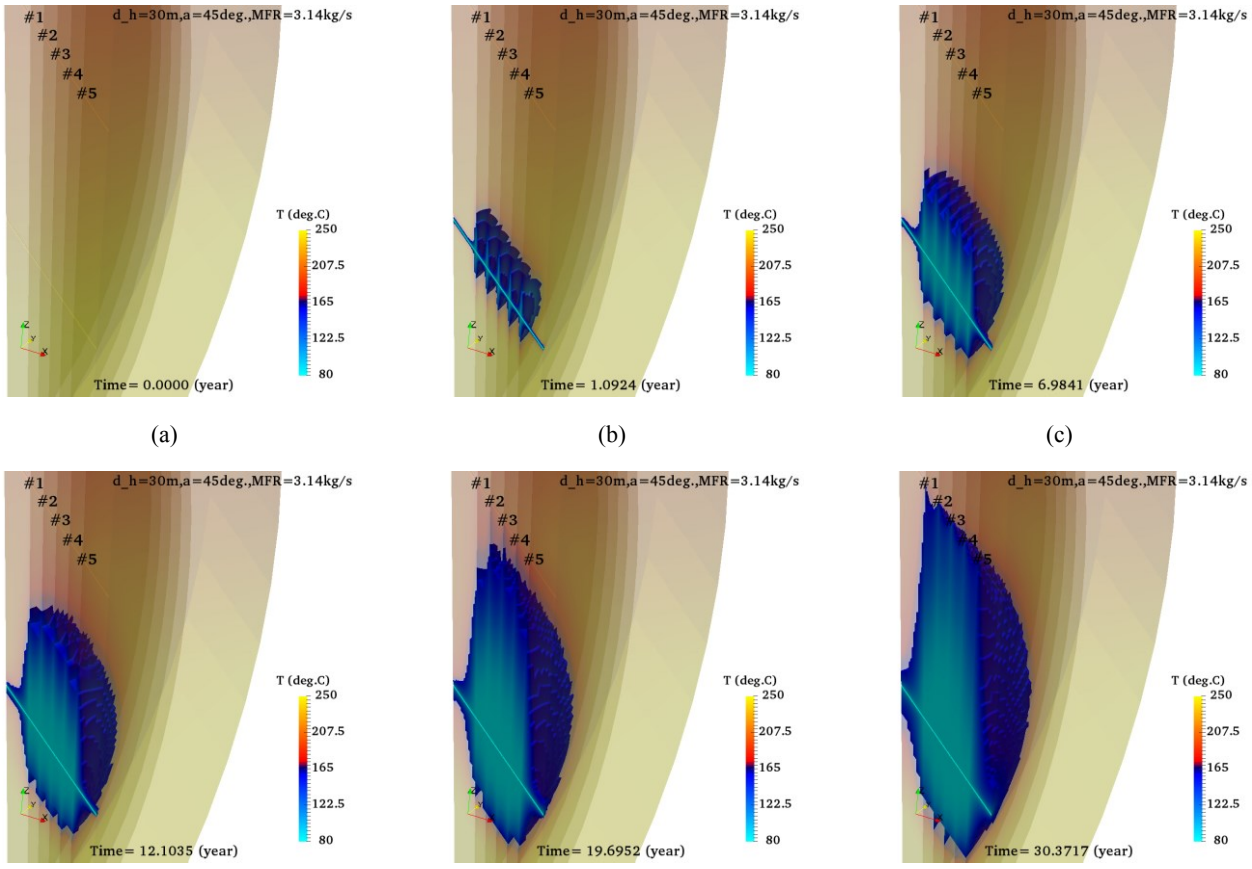

(a) (b) (c)

(d) (e) (f)

Figure 10: Evolution of the low-temperature regions in the reservoir ($d_h = 30$m, $\alpha = 45°$, q'_w=3.14kg/s).

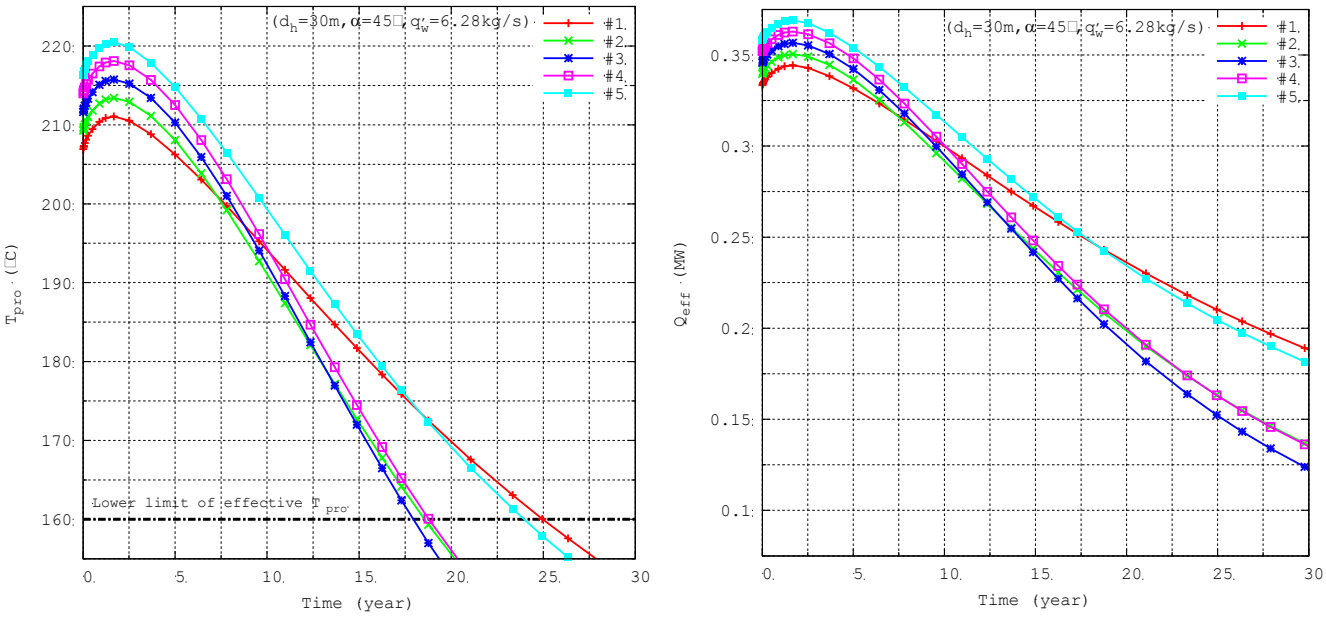

(a) (b)

Figure 11: Time histories of (a) the produced fluid temperature from the five production boundaries, and (b) the corresponding useful electric power rates ($d_h = 30$m, $\alpha = 45°$, q'_w=6.28kg/s).

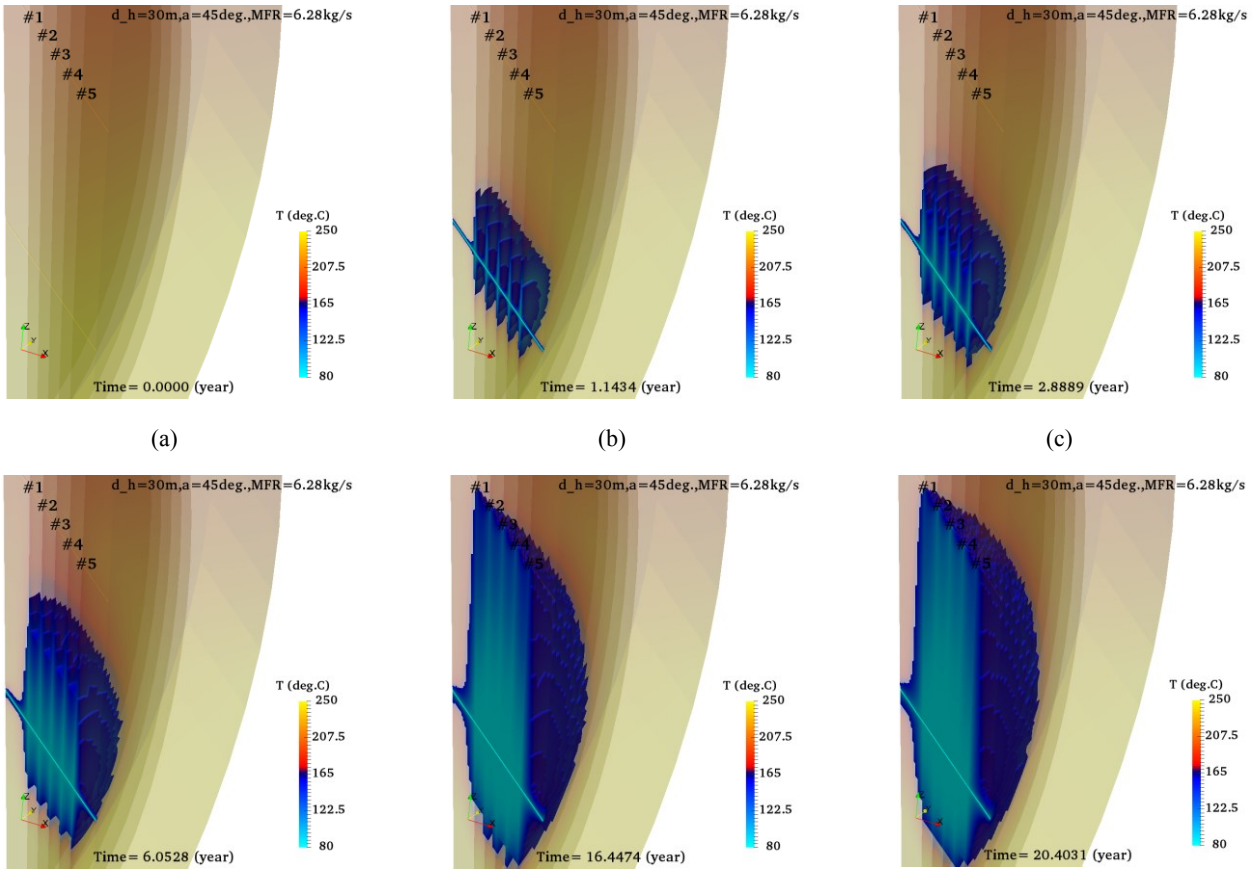

(a) (b) (c)

(d) (e) (f)

Figure 12: Evolution of the low-temperature regions in the reservoir ($d_h = 30$m, $\alpha = 45°$, q'_w=6.28kg/s).

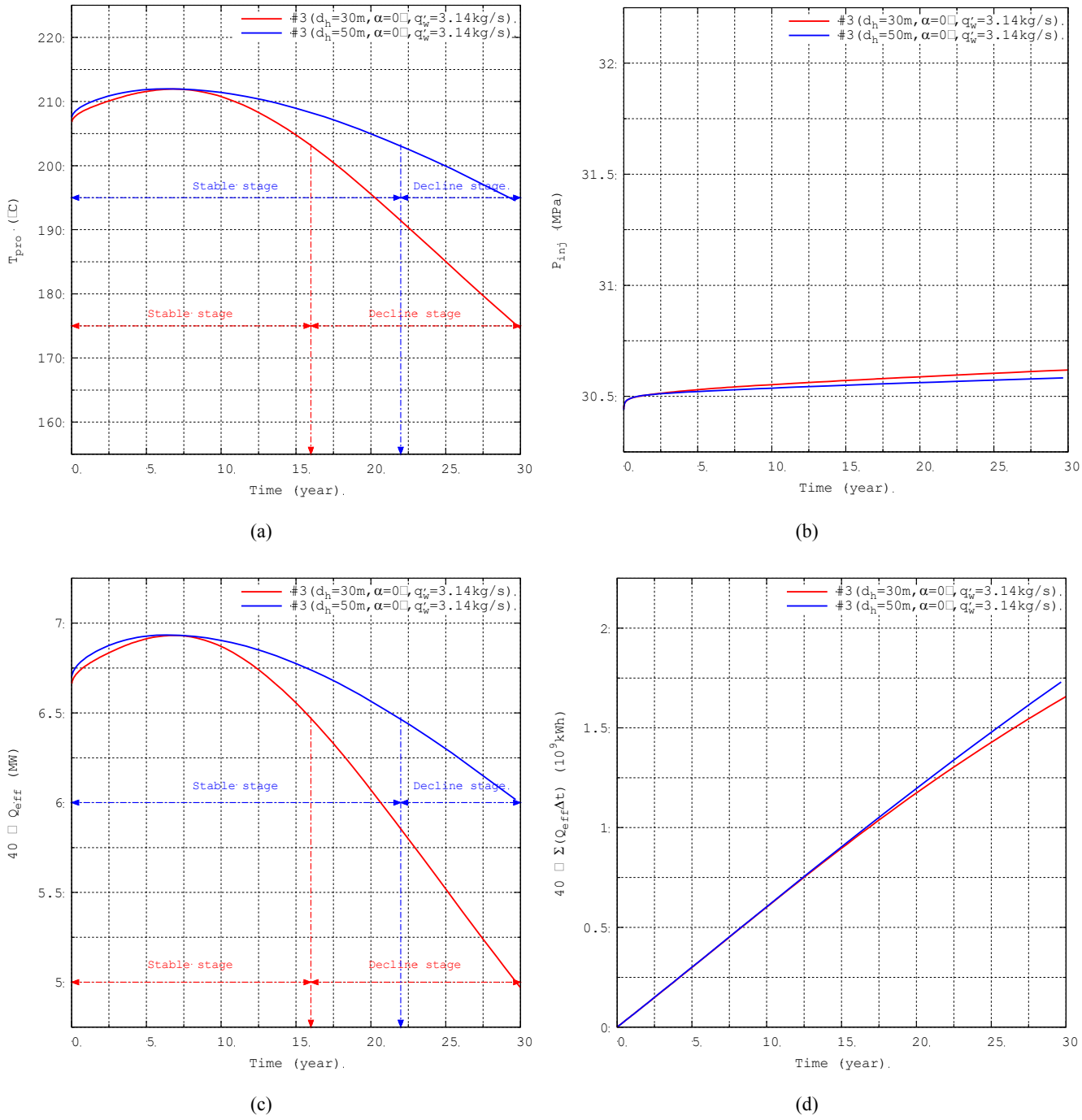

Figure 13: Sensitivity of the fracture horizontal spacing, d_h, on the performance of heat production over a 30-year period, with the well deviation angle and flow rate kept identical.

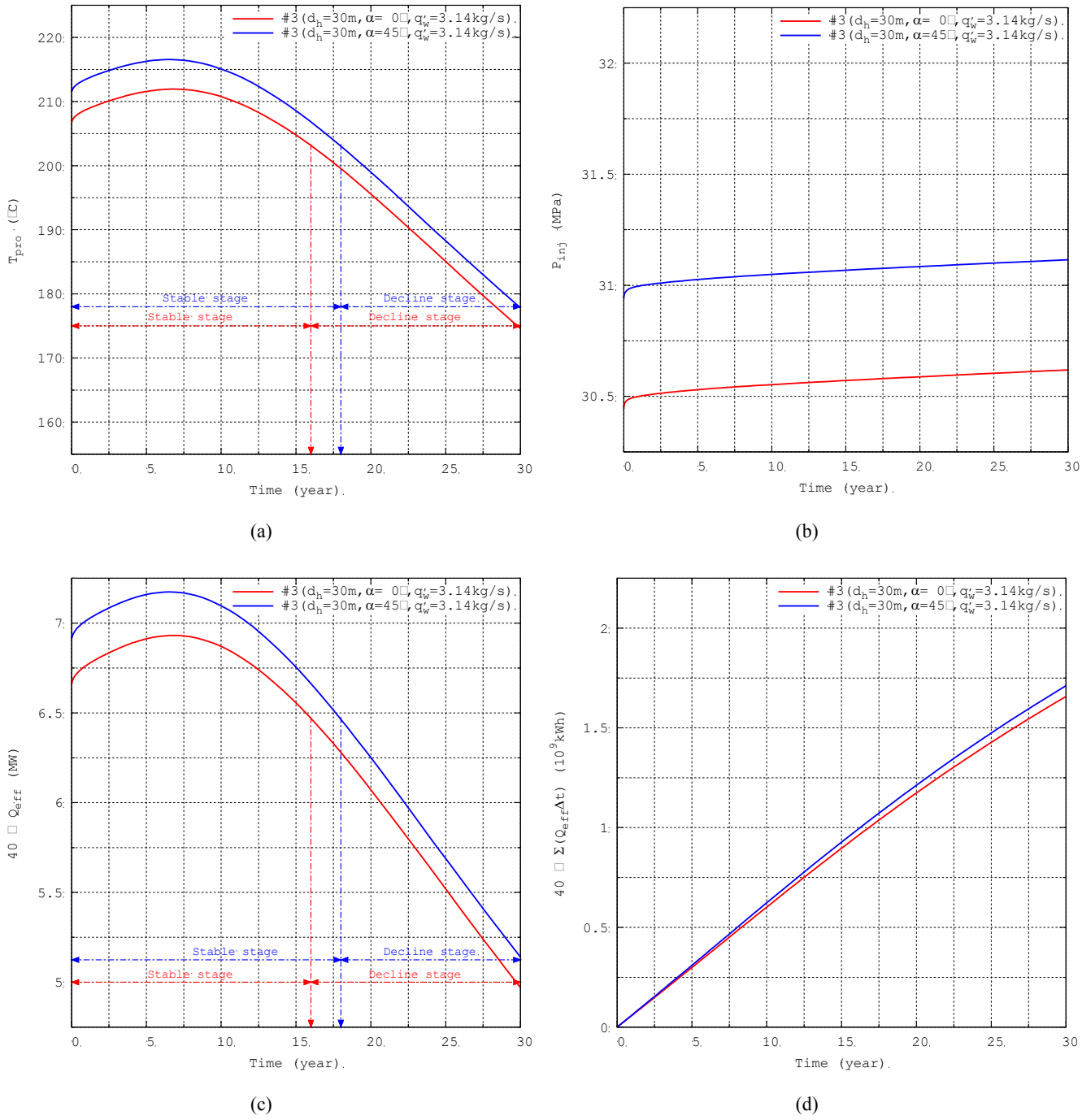

Figure 14: Sensitivity of the well deviation angle, α, on the performance of heat production over a 30-year period, with the fracture horizontal spacing and flow rate kept identical.

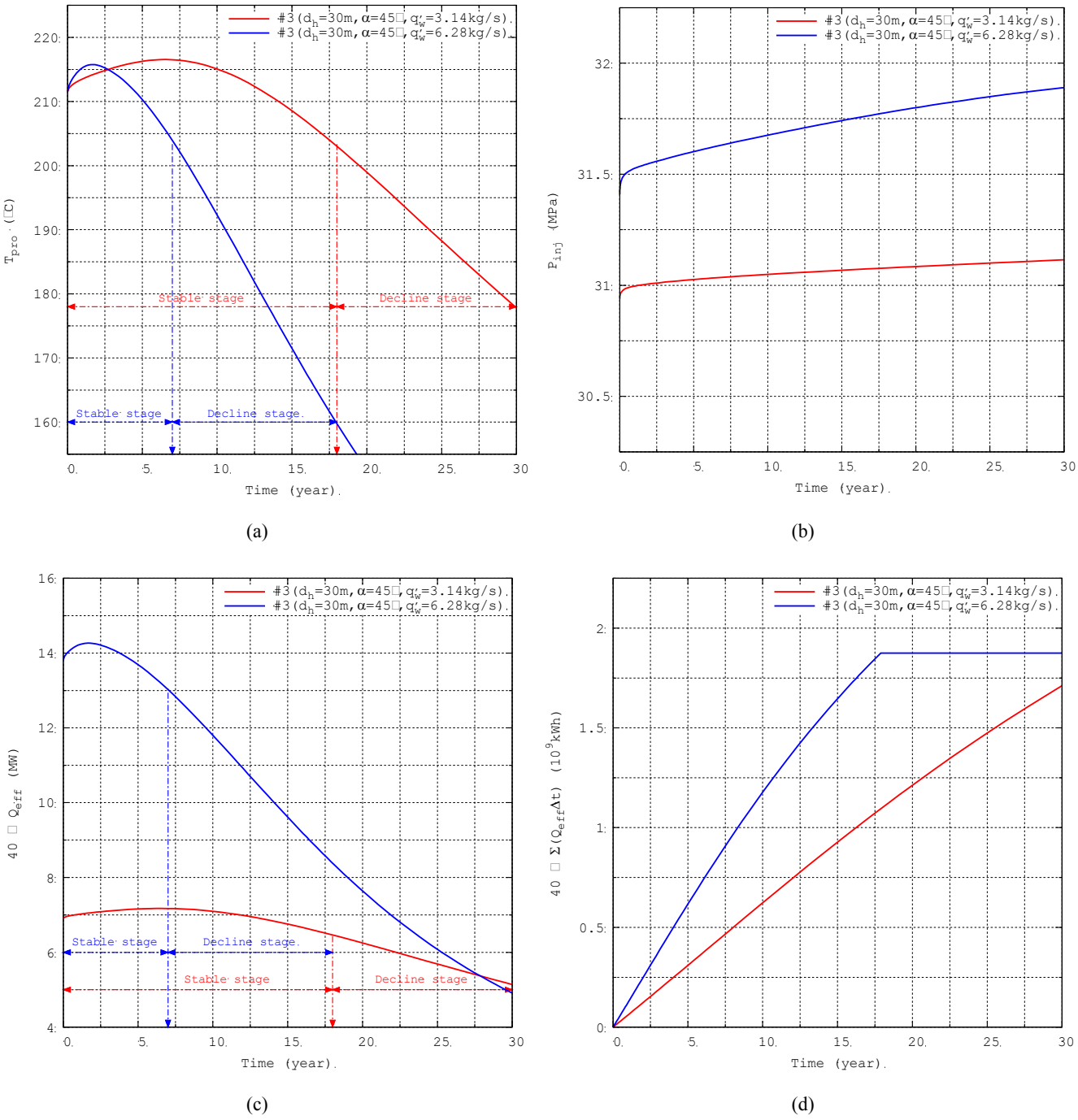

Figure 15: Sensitivity of the mass flow rate per fracture, q'_w on the performance of heat production over a 30-year period, with the fracture horizontal spacing and well deviation angle kept identical.

6. CONCLUSIONS

This work has presented a numerical assessment of the performance of heat production process over a 30-year period in a conceptual EGS model with a geothermal gradient of 65K per km depth in the reservoir, in which the water is circulated through a pair of parallel wells connected by a set of single large wing fractures. The simulation results have shown that a desirable output electric power rate and production lifespan could be obtained under suitable material properties and EGS operation parameters. Observations of a sensitivity analysis on some primary design constraints and parameters include the three aspects: 1) the equidistant horizontal spacing between the large single wing fractures has a profound effect on the long-term performance of heat production, 2) the downward deviation angle for parallel doublet wells may help overcome the possible difficulty of vertical drilling to reach a favorable production temperature, and 3) the thermal energy production rate and lifespan of the EGS has close dependency on the production flow rate. The numerical results also indicate that the EGS energy production rate and lifespan can be improved when the horizontal fracture spacing, well deviation angle, and production flow rate are under reasonable conditions. To enable the geothermal reservoir modeling and simulations in this work, an open-source, finite element based, fully implicit, fully coupled hydrothermal code, namely FALCON, has been developed and used in the test cases. Compared with most other existing codes that are either closed-source or commercially available in this area, this new open-source code has demonstrated a code development strategy that aims to provide an unparalleled easiness for user customization and multi-physics coupling. Test results have shown that the FALCON code is able to undertake the long-term tests very efficiently and accurately, thanks to the state-of-the-art nonlinear and linear solver algorithms implemented in the finite element framework of the code. In future, we are panning to implement a geo-mechanics module in the FALCON code, in order to deliver a fully-coupled, fully-implicit thermo-hydro-mechanical (THM) simulation capability in a single open-source code, and thus to support more complex EGS conceptual modeling and validation problems.

ACKNOWLEDGEMENT

The work described in this paper was supported by the U.S. Department of Energy, under DOE Idaho Operations Office Contract. Accordingly, the U.S. Government retains a nonexclusive, royalty-free license to publish or reproduce the published form of this contribution, or allow others to do so, for U.S. Government purposes. This information was prepared as an account of work associated by an agency of the U.S. Government. Neither the U.S. Government nor any agency thereof, nor any of their employees, makes any warranty, express or implied, or assumes any legal liability or responsibility for the accuracy, completeness, or usefulness of any information, apparatus, product, or process disclosed, or represents that its use would not infringe privately owned rights. References herein to any specific commercial product, process, or service by trade name, trademark, manufacturer, or otherwise, does not necessarily constitute or imply its endorsement, recommendation, or favoring by the U.S. Government or any agency thereof. The views and opinions of authors expressed herein do not necessarily state or reflect those of the U.S. Government or any agency thereof.

REFERENCES

Avdonin, N. A. (1964): Some Formulas for Calculating the Temperature Field of a Stratum Subject to Thermal Injection, *Neft'i Gaz*, 3, 37-41.

Bahrami, D., Danko, G., Fu, P., Guo, B., Podgorney, R., White, M., & Xia, Y. (2015): Poroelastic and Self-Propped Single Fracture THM Models for EGS Studies, *In proceedings of the 40th Stanford Geo-thermal Workshop*, Stanford, California, USA.

Balay, S., Abhyankar, S., Adams, M., Brown, J., Brune, P., Buschelman, K., ... and et al. (2014): PETSc Users Manual Revision 3.5 (No.ANL-95/11 Rev. 3.5), Argonne National Laboratory.

Banks, D. (2012): An Introduction to Thermo Geology: Ground Source Heating and Cooling, John Wiley & Sons.

Barbier, E. (2002): Geothermal Energy Technology and Current Status: An Overview, *Renewable and Sustainable Energy Reviews*, 6(1), 3-65.

Batchelor, A. S. (1981): The Creation of Hot Dry Rock Systems by Combined Explosive and Hydraulic Fracturing, *In proceedings of the International Conference on Geothermal Energy*, May 1982. Florence, Italy. *BHRA Fluid Eng. Bedford* (1982), pp. 321-342.

Blacker, T. D., Bohnhoff, W. J., & Edwards, T. L. (1994): CUBIT Mesh Generation Environment. Volume 1: Users Manual (No. SAND--94-1100). Sandia National Labs., Albuquerque, NM (United States).

Blackwell, D. D., Kelley, S., & Steele, J. L. (1992): Heat Flow Modeling of the Snake River Plain, Idaho. *US Department of Energy Report for Contract DE-AC07-761DO1570, 109*.

Brooks, A. N., & Hughes, T. J. (1982): Streamline Upwind/Petrov-Galerkin Formulations for Convection Dominated Flows with Particular Emphasis on the Incompressible Navier-Stokes Equations, *Computer Methods in Applied Mechanics and Engineering*, 32(1), 199-259.

Brownell, D. H., Garg, S. K., & Pritchett, J. W. (1977): Governing Equations for Geothermal Reservoirs. *Water Resources Research*, 13(6), pp. 929-934.

Bujakowski, W., Barbacki, A., Miecznik, M., Pająk, L., Skrzypczak, R., & Sowiżdżał, A. (2015): Modeling Geothermal and Operating Parameters of EGS Installations in the Lower Triassic Sedimentary Formations of the Central Poland Area, *Renewable Energy*, 80, 441-453.

Chen, J., & Jiang, F. (2015): Designing Multi-Well Layout for Enhanced Geothermal System to Better Exploit Hot Dry Rock Geothermal Energy, *Renewable Energy*, 74, 37-48.

Chen, J., & Jiang, F. (2016): A Numerical Study of EGS Heat Extraction Process Based on a Thermal Non-Equilibrium Model for Heat Transfer in Subsurface Porous Heat Reservoir, *Heat and Mass Transfer*, 52(2), 255-267.

Codina, R. (1998): Comparison of Some Finite Element Methods for Solving the Diffusion-Convection-Reaction Equation, *Computer Methods in Applied Mechanics and Engineering*, 156(1), 185-210.

Conti, J., Holtberg, P., Doman, L. E., Smith, K. A., Sullivan, J. O., Vincent, K. R., ... & Murphy, E. B. T. (2011): International Energy Outlook 2011. *U.S. Energy Information Administration*, Tech. Repo., No. DOE/EIA-0484.

Cooper, J. R., & Dooley, R. B. (2008): Release of the IAPWS Formulation 2008 for the Viscosity of Ordinary Water Substance.

Cornet, F. H. (1989): Experimental Investigations of Forced Fluid Flow through a Granite Rock Mass. *In proceedings of 4th International Seminar on the Results of EC Geothermal Energy Demonstration, Florence*, Italy, April 27-30, 1989, pp. 189-204.

Do Carmo, E. G. D., & Galeão, A. C. (1991): Feedback Petrov-Galerkin Methods for Convection-Dominated problems, *Computer Methods in Applied Mechanics and Engineering*, 88(1), 1-16.

Duchane, D. (1990): Hot Dry Rock: A Realistic Energy Option, *Bulletin of the Geothermal Resources Council*, 19(3), 83-88.

Duchane, D., & Brown, D. (2002): Hot Dry Rock (HDR) Geothermal Energy Research and Development at Fenton Hill, New Mexico, *Geothermal Heat Center Bulletin*.

Evans, K. (2010): Enhanced/Engineered Geothermal System: An Introduction with Overviews of Deep Systems Built and Circulated to Date, *In China Geothermal Development Forum*, Beijing, China (pp. 395-418).

Faust, C. R., & Mercer, J. W. (1979a): Geothermal Reservoir Simulation: 1. Mathematical Models for Liquid- and Vapor-Dominated Hydrothermal Systems, *Water Resources Research*, 15(1), 23-30.

Faust, C. R., & Mercer, J. W. (1979b): Geothermal reservoir simulation: 2. Numerical Solution Techniques for Liquid- and Vapor-Dominated Hydrothermal Systems, *Water Resources Research*, 15(1), 31-46.

Gaston, D., Newman, C., Hansen, G., & Lebrun-Grandie, D. (2009): MOOSE: A Parallel Computational Framework for Coupled Systems of Nonlinear Equations. *Nuclear Engineering and Design*, 239(10), 1768-1778.

Graf, T. (2009): Simulation of Geothermal Flow in Deep Sedimentary Basins in Alberta, *Alberta Energy Resources Conservation Board*.

Hascoet, L., & Pascual, V. (2013): The Tapenade Automatic Differentiation Tool: Principles, Model, and Specification, *ACM Transactions on Mathematical Software (TOMS)*, 39(3), 20.

Held, S., Genter, A., Kohl, T., Kölbel, T., Sausse, J., & Schoenball, M. (2014): Economic Evaluation of Geothermal Reservoir Performance through Modeling the Complexity of the Operating EGS in Soultz-sous-Forêts, *Geothermics*, 51, 270-280.

ITASCA Consulting Group (1997): FALC 3D, Fast Lagrangian Analysis of Continua in 3 Dimensions, Version 2.0.

Jiang, F., Chen, J., Huang, W., & Luo, L. (2014): A Three-Dimensional Transient Model for EGS Subsurface Thermo-Hydraulic Process, *Energy*, 72, 300-310.

Jiang, F., Luo, L., & Chen, J. (2013): A Novel Three-Dimensional Transient Model for Subsurface Heat Exchange in Enhanced Geothermal Systems, *International Communications in Heat and Mass Transfer*, 41, 57-62.

Jung, R. (2013): EGS – Goodbye or Back to the Future, *in proceedings of International Society for Rock Mechanics (ISRM) International Conference for Effective and Sustainable Hydraulic Fracturing*, Brisbane, Australia.

Kirk, B. S., Peterson, J. W., Stogner, R. H., & Carey, G. F. (2006): libMesh: A C++ Library for Parallel Adaptive Mesh Refinement/Coarsening Simulations. *Engineering with Computers*, 22(3-4), 237-254.

Knoll, D. A., & Keyes, D. E. (2004): Jacobian-Free Newton–Krylov Methods: A Survey of Approaches and Applications, *Journal of Computational Physics*, 193(2), 357-397.

Kohl, T., & Hopkirk, R. J. (1995): "FRACure" – A Simulation Code for Forced Fluid Flow and Transport in Fractured, Porous Rock, *Geothermics*, 24(3), 333-343.

McClure, M. W., & Horne, R. N. (2014): An Investigation of Stimulation Mechanisms in Enhanced Geothermal Systems, *International Journal of Rock Mechanics and Mining Sciences*, 72, 242-260.

McDermott, C. I., Randriamanjatosoa, A. R., Tenzer, H., & Kolditz, O. (2006): Simulation of Heat Extraction from Crystalline Rocks: The Influence of Coupled Processes on Differential Reservoir Cooling, *Geothermics*, 35(3), 321-344.

Murphy, H. D. (1985): Hot Dry Rock Phase II Reservoir Engineering, *Tech. Repo*. (No. LA-UR-85-3334). Los Alamos National Laboratory, New Mexico, USA.

Olasolo, P., Juárez, M. C., Morales, M. P., & Liarte, I. A. (2016): Enhanced Geothermal Systems (EGS): A Review, *Renewable and Sustainable Energy Reviews*, 56, 133-144.

Podgorney, R., Huang, H., & Gaston, D. (2010): A Fully Coupled, Implicit, Finite Element Model for Simultaneously Solving Multiphase Fluid Flow, Heat Transport, and Rock Deformation. *Geothermal Resources Council Transactions*, 34: 427-432.

Polsky, Y., Capuano, L., Finger, J., Huh, M., Knudsen, S., Mansure, A. J., ... & Swanson, R. (2008): Enhanced Geothermal Systems (EGS) Well Construction Technology Evaluation Report. *Sandia National Laboratories, Sandia Report*, SAND2008-7866, 1-108.

Pruess, K., Oldenburg, C. M., & Moridis, G. J. (1999): TOUGH2 User's Guide Version 2, Lawrence Berkeley National Laboratory.

Rutqvist, J., Wu, Y. S., Tsang, C. F., & Bodvarsson, G. (2002): A Modeling Approach for Analysis of Coupled Multiphase Fluid Flow, Heat Transfer, and Deformation in Fractured Porous Rock, *International Journal of Rock Mechanics and Mining Sciences*, 39(4), 429-442.

Smith, M. C., Aamodt, R. L., Potter, R. M., & Brown, D. W. (1975): Manmade Geothermal Reservoirs, *Tech. Repo. No. LA-UR-75-953. CONF-750525-6*. Los Alamos Scientific Laboratory, New Mexico, USA.

Tester, J. W., Brown, D. W., & Potter, R. M. (1989): Hot Dry Rock Geothermal Energy – A New Energy Agenda for the 21st Century, *Tech. Repo. No. LA-11514-MS*. Los Alamos National Laboratory, New Mexico, USA.

Wagner, W., Cooper, J. R., Dittmann, A., Kijima, J., Kretzschmar, H. J., Kruse, A., & Willkommen, T. (2000): The IAPWS industrial formulation 1997 for the thermodynamic properties of water and steam, *Journal of Engineering for Gas Turbines and Power*, 122(1), 150-184.

Hughes, T. J., Franca, L. P., & Mallet, M. (1986a): A New Finite Element Formulation for Computational Fluid Dynamics: I. Symmetric Forms of the Compressible Euler and Navier-Stokes Equations and the Second Law of Thermodynamics, *Computer Methods in Applied Mechanics and Engineering*, 54(2), 223-234.

Hughes, T. J., Mallet, M., & Akira, M. (1986b): A New Finite Element Formulation for Computational Fluid Dynamics: II. Beyond SUPG, *Computer Methods in Applied Mechanics and Engineering*, 54(3), 341-355.

Reichenberger, V., Jakobs, H., Bastian, P., & Helmig, R. (2006): A Mixed-Dimensional Finite Volume Method for Two-Phase Flow in Fractured Porous Media, *Advances in Water Resources*, 29(7), 1020-1036.

Sanyal, S. K., & Butler, S. J. (2005): An Analysis of Power Generation Prospects from Enhanced Geothermal Systems, *Geothermal Resources Council Transactions*, 29, 131-8.

U.S. Department of Energy Office of Energy Efficiency & Renewable Energy (2008): An Evaluation of Enhanced Geothermal Systems Technology, <https://www1.eere.energy.gov/geothermal/pdfs/evaluation_egs_tech_2008.pdf> [Accessed February 2016].

Xia, Y., & Podgorney, R. (2015a): FALCON, a Finite Element Geothermal Reservoir Simulation Code by Idaho National Laboratory, source code available at < https://github.com/idaholab/falcon > [Accessed February 2016].

Xia, Y., Podgorney, R., & Huang, H. (2015b): Assessment of a Hybrid Continuous / Discontinuous Galerkin Finite Element Code for Geothermal Reservoir Simulations, *Rock Mechanics and Rock Engineering*, submitted, under review.

Xing, H., Liu, Y., Gao, J., & Chen, S. (2015): Recent Development in Numerical Simulation of Enhanced Geothermal Reservoirs, *Journal of Earth Science*, 26(1), 28-36.

Zeng, Y. C., Su, Z., & Wu, N. Y. (2013a): Numerical Simulation of Heat Production Potential from Hot Dry Rock by Water Circulating through Two Horizontal Wells at Desert Peak Geothermal Field, *Energy*, 56, 92-107.

Zeng, Y. C., Wu, N. Y., Su, Z., Wang, X. X., & Hu, J. (2013b): Numerical Simulation of Heat Production Potential from Hot Dry Rock by Water Circulating through a Novel Single Vertical Fracture at Desert Peak Geothermal Field, *Energy*, 63, 268-282.

Zyvoloski, G. (2007): FEHM: A Control Volume Finite Element Code for Simulating Subsurface Multi-Phase Multi-Fluid Heat and Mass Transfer, *Los Alamos Unclassified Report LA-UR-07-3359*.

APPENDIX A. FALCON CODE DESCRIPTION

The FALCON code developed a set of “physics” kernels handling each term in the weak formulation of the mass conservation equation in Eq. (9) and energy conservation equation in Eq. (10), as well as a set of ”Auxiliary” and ”Material” kernels for equations of state (EOS) and flow-transport properties required for geothermal reservoir simulations. As will be shown in the sections that follow, these kernels all have modular, pluggable structures, and can be coupled in arbitrary ways depending on the type of problems of interest. It is also worth noting that the MOOSE framework provides a material kernel. Flow and transport properties such as porosity, permeability, and relative permeability can all be defined within this material kernel and can be accessed by the physics kernels during each residual evaluation.

A.1 Kernels

As mentioned above, FALCON uses kernels to describe each term to be calculated on the quadrature point (QP) of an element or face in the weak formulation of governing PDE. Here we present the kernels written to date, beginning with the primary physics kernels (including the Dirac kernels), boundary conditions kernels, material kernels, auxiliary kernels, and lastly postprocessor kernels.

A.1.1 Physics and Dirac Kernels

The physics kernels and Dirac Kernels for the mass conservation equation in Eq. (9) and energy conservation equation in Eq. (13) are summarized in Table 3. A total of three kernels can be used to describe each of the governing PDEs. For mass conservation, the governing PDE is broken into two physics kernels – the time derivative term, **PTMassTimeDerivative**, and mass flux term, **PTMassResidual** that consists of contribution from fluid pressure gradient and gravitational force; and one Dirac kernel – the point mass source/sink term, **PTMassPointSource**. For energy conservation, the governing PDE is also broken into two physics kernels – the time derivative term, **PTEnergyTimeDerivative**, and energy flux term, **PTEnergyResidual** that consists of conductive flux, convective flux, and stabilization terms; and one Dirac kernel – the point energy source/sink term, **PTEnergyPointSource**.

Table 3: Summary of FALCON's Physics Kernels and Dirac Kernels for mass conservation, and energy conservation.

Kernel	*Description*
PTMassTimeDerivative	Calculate the time derivative term of mass conservation equation, $\frac{\mathrm{d}p}{\mathrm{d}t}\phi\frac{\partial\rho_{\mathrm{w}}}{\partial p}W_h$, on QP.
PTMassResidual	Calculate the mass flux term of mass conservation equation, $-\mathbf{q}_{\mathrm{M}}\cdot\nabla W_h$, on QP.
PTMassPointSource	Calculate the point mass source/sink term of mass conservation equation, $-\acute{q}W_h$, on QP.
PTEnergyTimeDerivative	Calculate the time derivative term of energy conservation equation, $\frac{\mathrm{d}T}{\mathrm{d}t}C_{\mathrm{m}}W_h$, on QP.
PTEnergyResidual	Calculate the flux term of energy conservation equation, $(K_m\nabla T - T\mathbf{q}_{\mathrm{E}})\cdot\nabla W_h + R_E(\tau_1\mathbf{q}_{\mathrm{E}} + \tau_2\mathbf{q}_{\mathrm{E}_{\parallel}})\cdot\nabla W_h$, on QP.
PTEnergyPointSource	Calculate the point energy source/sink term of energy conservation equation, $-\acute{Q}W_h$, on QP.

A.1.2 Boundary Condition Kernels

Five boundary condition (BC) kernels have been written as part of the FALCON code, as summarized in Table 4. The **DirichletBC** kernel is directly inherited from MOOSE, requiring no modifications for use in FALCON. To apply these BCs, one must simply specify the boundary, the variable, and either a scalar value of the variable or the gradient of the variable normal to the boundary. These kernels are easy to implement, and capable of handling most conditions needed for reservoir simulation.

Table 4: Summary of FALCON's Boundary Condition Kernels for mass conservation, and energy conservation.

Kernel	*Description*
DirichletBC	Impose a user-input variable value on a specific boundary surface. This BC kernel is provided by MOOSE framework, and can be used to specify pressure and temperature, respectively.
PTMassFluxBC	Impose a user-input mass flux value, $\mathbf{q}_{\mathrm{M}}\cdot\mathbf{n}$ normal to a specific boundary surface. A positive value means injection, while a negative value means production.
PTMassFreeBC	Impose a free flow exit normal to a specific boundary surface, where the $\mathbf{q}_{\mathrm{M}}$ value is interpolated from the host element to the surface quadrature point.
PTEnergyInflowBC	Impose an energy influx normal to a specific boundary surface, $(-K_{\mathrm{m}}\nabla T + T\mathbf{q}_{\mathrm{E}})\cdot\mathbf{n}$, where T is an user-input, but ∇T is interpolated from the host element to the surface quadrature point.
PTEnergyOutflowBC	Impose an energy out-flux normal to a specific boundary surface, $(-K_{\mathrm{m}}\nabla T + T\mathbf{q}_{\mathrm{E}})\cdot\mathbf{n}$. Both T and ∇T are interpolated from the host boundary element to the surface quadrature point.

A.1.3 Material Kernels

The material kernels are used to calculate the material properties specific to the physics being resolved. In the FALCON code, the material kernel, **PTGeothermal**, has been developed to calculate 1) material properties of the porous medium (e.g., permeability, porosity), 2) thermodynamic properties of the liquid-phase water, and 3) some coefficients required in the stabilization term of the energy conservation equation, as summarized in Table 5. **PTGeothermal** is designed such that most of the derived scalar and vector variables required in

multiple kernels (e.g., C_{m}, $\mathbf{q}_{\mathrm{M}}$, and $\mathbf{q}_{\mathrm{E}}$.) are calculated only once in **PTGeothermal** and stored, which avoids the redundant calculations of those quantities in other kernels.

Table 5: Summary of FALCON's Material Kernels

Kernel	*Description*
PTGeothermal	User-input material properties include: reference temperature, intrinsic permeability, porosity, total compressibility of porous medium, density of rock, density of fluid, viscosity of fluid, magnitude of gravity, unit directional vector of gravity, specific heat capacity of rock, specific heat capacity of fluid, medium average thermal conductivity, and a constant pressure gradient. The default values of these quantities will be used if users do not specify them. Three options for the "fluid property formulation" entry are available: 1) "constant", 2) "compressibility", and 3) "wseos". For "constant", the default or user-input material property values are used; For "compressibility", the density and viscosity of water are calculated by the temperature based functions in Eq. (7) and (8), respectively, and $\frac{\partial \rho_{\mathrm{w}}}{\partial p} = \rho_{\mathrm{w}} C_{\mathrm{t}}$ is used, where the total compressibility of porous medium, C_{t} is a user-input parameter; For "wseos", the density and viscosity of water are calculated through the WSEOS process. Remark 1: If no nonlinear variable name is specified to the "temperature" entry, the default or user-input reference temperature value will be used when needed. This makes the use of Eq. (7) and (8), or WSEOS possible when the mass conservation equation is being solved in an isothermal condition. Four options for the "stabilizer" entry are available for the energy conservation equation: 1) "none", 2) "zero", 3) "supg", and 4) "supg_dc". For "none", the original equation in Eq. (10) is solved; For "zero", the original equation in Eq. (10) is solved, with the convection term being neglected; For "supg", a standard SUPG stabilized formulation in Eq. (12) is solved; For "supg_dc", the SUPG Discontinuity Capturing stabilized formulation in Eq. (13) is solved.

A.1.4 Auxiliary Kernels

The main functionality of auxiliary kernels is to calculate the physical properties of fluid. Usually, auxiliary kernels are not the required components of simulations, but are often used to output the fluid properties for diagnostic purposes, e.g., the Darcy flux, and fluid velocity. The auxiliary kernels that have been developed for the FALCON code are summarized in Table 6.

Table 6: Summary of FALCON's Auxiliary Kernels

Kernel	*Description*
PTDarcyFluxAux	Calculate the *x*-, or *y*-, or *z*-direction component of the Darcy flux vector in reservoir, $\mathbf{q}$. Users need to specify the corresponding auxiliary variable(s).
PTFluidVelocityAux	Calculate the *x*-, or *y*-, or *z*-direction component of the fluid velocity vector in reservoir, $\mathbf{q}/\phi$. Users need to specify the corresponding auxiliary variable(s).

A.1.5 Postprocessor Kernels

A postprocessor kernel conducts a "reduction" or "aggregation" calculation based on the solution variables, which results in a single scalar value. Usually, postprocessor kernels are not the required components of simulations, but are often used to output the aggregated information related to the reservoir performance, e.g., flow rate and total energy production rate of a wellbore. This feature also enables the implementation of any numerical algorithm that requires the aggregated data. The postprocessor kernels that have been developed for the FALCON code are summarized in Table 7.

Table 7: Summary of FALCON's Postprocessor Kernels

Kernel	*Description*
PTMassSideFluxIntegral	Calculate the flow rate ($\mathrm{kg \cdot s^{-1}}$) of a boundary surface specified as an injection or production wellbore.

PTMassSideFluxAverage	Calculate the area average flow rate ($kg \cdot m^{-2} \cdot s^{-1}$) of a boundary surface specified as an injection or production wellbore.
PTEnergySideProductionIntegral	Calculate the energy production rate ($J \cdot s^{-1}$) of a boundary surface defined as production wellbore.

A.2 Program Execution

FALCON is a complete application and has full control of its execution through a "main" entry subroutine as well a through a flexible "executioner" API. A typical program workflow, however, follows a fairly rigid set of operations that can be grouped into two major categories: problem setup and execution. Problem setup generally consists of reading an input file and construction of the various objects used during execution. These functions are all handled by the MOOSE library. During execution the library manages the states of dozens of internal variables and data structures necessary for the finite element calculations.

A.3 Restarting Simulations

FALCON support's a robust restart system. Solution files written during the simulation contain detailed information about each variable at each node point on the mesh for each time step. When restarting a simulation, variables used in the simulation can be initialized to any value from the previous system at any time step. Another advantage to the restart system is the ability to add additional variables to be solved. There are a few limitations to this system however. Internal state variables, material properties and other auxiliary values not explicitly stored in the solution file cannot be recovered for restart runs.